Direct Numerical Simulation of Turbulent Flows in a Rectangular Duct of Different Aspect Ratios

by

Jiaxin Yan

A Thesis submitted to the Faculty of Graduate Studies of
The University of Manitoba
in partial fulfilment of the requirements of the degree of

MASTER OF SCIENCE

Department of Mechanical Engineering
University of Manitoba
Winnipeg, Manitoba, Canada

I hereby declare that I am the sole author of this thesis.

I authorize the University of Manitoba to lend this thesis to other institutions or individuals for the purpose of scholarly research.

I further authorize the University of Manitoba to reproduce this thesis by photocopying or by other means, in total or in part, at the request of other institutions or individuals for the purpose of scholarly research.

The University of Manitoba requires the signatures of all persons using or photocopying this thesis. Please sign below, and give address and date.

Abstract

Direct numerical simulations are performed to investigate turbulent flows in a rectangular duct of aspect ratio varying from 1.0 to 3.0 at a fixed low Reynolds number 150. Persistent secondary flows of Prandtl's second kind are observed in the corners of the ducts. As the aspect ratio increases, streamwise vortices near the top and bottom walls extend towards to the central vertical plane of ducts. Particularly, the displacement of vortex cores near the top/bottom wall can be described as a function of the distance to the sidewall. Detailed analyses of turbulence statistics including the mean flow, turbulent kinetic energy, turbulent intensities, Reynolds stress budgets, and pre-multiplied one-dimensional energy spectrum are conducted to understand the aspect ratio effects on the flow physics. In the duct of aspect ratio 3.0, hairpin flow structures are present in the central regions of the duct, and their characteristics are similar to those exhibited in the plane channel flows. Furthermore, as indicated by the energy spectra, a spanwise quasi-homogeneous region spans over approximately 270 wall units in the central region of the rectangular duct.

Acknowledgements

This thesis is presented to the Department of Mechanical Engineering of University of Manitoba. I, Jiaxin Yan, as a master student of Mechanical Engineering, would first thank my academic advisor, Professor Bing-Chen Wang for offering me such a great opportunity to study computational fluid dynamics. I would also like to thank Dr. Xingjun Fang for his help on my code debugging, and his comments on my thesis drafts. Truly, I would like to thank my labmates in office E1-427 during my master program for their friendship and help. Finally, I thank my father Zhe Yan, my mother Li Zhang, and my wife Bing Yang, for their unconditional love and supports.

Table of Contents

List of Tables

List of Figures

Nomenclature

English Symbols

a_{ij}	velocity gradient tensor: $\partial u_i/\partial x_j$
a'_{ij}	velocity fluctuation gradient tensor: $\partial u'_i/\partial x_j$
D_{ij}	diffusion term for Reynolds stresses
H_{ij}	convection term for Reynolds stresses
k	turbulent kinetic energy
L_x	duct length
L_y	duct height
L_z	duct width
P_k	production term for TKE
P_{ij}	production term for Reynolds stresses
$Q2$	second quadrant event, ejection
$Q4$	fourth quadrant event, sweep
R_{uu}	two-point autocorrelation coefficient of velocity fluctuation u'
R_{vv}	two-point autocorrelation coefficient of velocity fluctuation v'
R_{ww}	two-point autocorrelation coefficient of velocity fluctuation w'
Re	Reynolds number: $u\delta/\nu$
Re_τ	Reynolds number: $u_\tau\delta/\nu$

Re_b	Reynolds number: $U_b\delta/\nu$
s_{ij}	strain-rate tensor: $(a_{ij} + a_{ji})/2$
s'_{ij}	fluctuation strain-rate tensor: $(a'_{ij} + a'_{ji})/2$
t	total flow time
U_0	centreline mean velocity
U_b	bulk mean velocity
u_{cs}	cross-stream velocity: $\sqrt{\langle v\rangle^2 + \langle w\rangle^2}$
$u_{\tau,\text{avg}}$	averaged wall friction velocity
$u_{\tau,\text{local}}$	local wall friction velocity
u, v, w	velocity components in x, y and z directions, respectively
x, y, z	streamwise, vertical and spanwise directions, respectively

Greek Letters

δ	half duct height
δ_{ij}	Kronecker delta
ε_{ijk}	Levi-Civita symbol
ε_{ij}	dissipation term for Reynolds stresses
β	Streamwise wavelength
ν	kinematic viscosity
ν_t	turbulent eddy viscosity
ω_1	vorticity in x direction: $\partial w/\partial y - \partial v/\partial z$
ω_2	vorticity in y direction: $\partial u/\partial z - \partial w/\partial x$
ω_3	vorticity in z direction: $\partial v/\partial x - \partial u/\partial y$
θ	inclination angle of the principal axis of mean strain rate tensor s_{ij}

λ_{ci}	turbulent swirling strength
λ_x	streamwise wavelength
Π	mean streamwise pressure gradient
Π_{ij}	pressure-strain term for Reynolds stresses
τ_w	wall shear stress
ϕ_{uu}	pre-multiplied one dimensional energy spectrum of u'
ϕ_{vv}	pre-multiplied one dimensional energy spectrum of v'
ϕ_{ww}	pre-multiplied one dimensional energy spectrum of w'

Subscripts and Superscripts

$(\cdot)^+$, $\langle\cdot\rangle^+$	quantity in wall coordinates
$(\cdot)^b$	quantity at the bottom wall
$(\cdot)^t$	quantity at the top wall
$(\cdot)^s$	quantity at the sidewall
$(\cdot)_1$, $(\cdot)_2$, $(\cdot)_3$	Streamwise, vertical and spanwise components, respectively
$(\cdot)_i$, $(\cdot)_j$, $(\cdot)_{ij}$	vectors or second-order tensors: $i, j = 1, 2, 3$
$\langle\cdot\rangle$	time- and space-averaged quantity
$(\cdot)'$	fluctuation component
$(\cdot)_{\text{rms}}$	Root-mean-square
$\hat{(\cdot)}$	quantity in Fourier space

Abbreviations

1-D	one-dimensional
2-D	two-dimensional
3-D	three-dimensional
AR	aspect ratios (duct width to height)
CCW	counter clockwise
CFD	computational fluid dynamics
CFL	Courant-Friedrichs-Lewy
CW	Clockwise
DNS	direct numerical simulation
GLL	Gauss-Lobatto-Legendre
HVAC	heating, ventilation and air conditioning
LES	large-eddy simulation
LETOT	large-eddy turnover time
MPI	message passing interface
MWR	Method of weighted residual
RMS	Root-mean-squares
SEM	spectral-element method
TKE	turbulence kinetic energy
ZPG	zero-pressure-gradient

Chapter 1

Introduction

1.1 Backgrounds

Turbulent rectangular duct flow is encountered in many engineering applications such as heating, ventilation and air conditioning (HVAC). Due to space limitations and concerns of noise, the aspect ratios (AR, the ratio of width to height) of rectangular ducts used in HVAC systems are typically lower than 3.0 (Bhatia, 2018). For these low aspect ratios of rectangular ducts, strong interactions between turbulent boundary layers developed over all four walls are present. Particularly, due to inhomogeneity in the cross-section of the duct, secondary flows in the form of streamwise vortices occur, which further alter wall shear stresses and heat transfer performances. In order to optimize the design of flow path in HVAC, it is of interest to conduct a detailed investigation of AR effects on turbulent flows confined within rectangular ducts.

1.2 Literature review

In this section, a review of relevant literatures is presented, which focuses on three key subjects: secondary flows in a rectangular duct flow, the AR effects on the flow field, and coherent flow structures and minimal domain for capturing them in numerical simulations.

1.2.1 Secondary flows in rectangular ducts

In the literature, pressure-driven flows confined within closed square ducts have been extensively studied through experiments and numerical simulations. For instance, Prandtl (1926) observed the existence of secondary flows in the pattern of one pair of counter-rotating streamwise vortices in each corner of ducts. He speculated that the observed secondary flows were generated by the gradient of Reynolds stresses, a conclusion that was later confirmed and documented by Nikuradse (1930). Later, based on their results of Reynolds stress measured using hot-wire anemometers, Brundrett & Baines (1964) demonstrated how turbulent kinetic energy (TKE) transfers between Reynolds normal stresses, facilitating the formation of the secondary flows. Furthermore, they pointed out that although the secondary flow permeates further into the corners with an increasing Reynolds number, its major characteristics were independent from Reynolds numbers (within the range of their investigation, from $20,000$ to $83,000$). This conclusion was further confirmed by Madabhushi & Vanka (1991) and Pinelli *et al.* (2010) through their large-eddy simulation (LES) and direct numerical simulation (DNS) studies, respectively. Gavrilakis (1992) conducted a DNS study of turbulent flows in a square duct at $Re_\tau = u_\tau \delta/\nu \approx 150$ (defined based on the friction velocity and the half duct height). He observed very long low-speed streaks similar to those exhibited in turbulent plane channel flows, and demonstrated how the computational domain size influences the predictive accuracy of turbulence statistics. Later, Huser & Biringen (1993) preformed DNS of turbulent square duct flow at $Re_\tau \approx 300$,

and demonstrated that the formation of secondary flow was essentially associated with the second-quadrant event (ejection) and the interactions of the boundary layers developed over the two nearby sidewalls. In their follow-up research, Huser *et al.* (1994) further emphasized that the anisotropy of Reynolds stresses was the key to promote secondary flows in a turbulent square duct. Vinuesa *et al.* (2014) conducted DNS study to investigate fully-developed turbulent flows confined within rectangular ducts of different AR values (ranging from 1.0 to 7.0) at $Re_\tau \approx 180$ and 330. They examined the minimum sampling time for secondary flows to achieve a statistically stationary state in a transient simulation.

1.2.2 Turbulent flows in rectangular ducts of different AR values

Turbulent Poiseuille flows in rectangular ducts of large values of AR have been studied extensively using experimental approaches. Laufer (1951) measured turbulence using hot wires in a rectangular duct of AR ≈ 12. He analyzed turbulent statistics at three Reynolds numbers of 2.05×10^4, 5.13×10^4, and 1.03×10^5 (defined base on the channel half-width and the maximum mean velocity, i.e., $Re = U_{\text{max}}\delta/\nu$). By employing different probe-tube and hot-wire measurement techniques (Deissler, 1954; Deissler & Taylor, 1956), Hartnett *et al.* (1962) investigated the friction coefficients in both laminar and turbulent rectangular duct flows at Reynolds numbers from 6×10^3 to 5×10^5 (defined based on bulk mean velocity and hydraulic diameter, i.e., $Re_h = U_b D_h/\nu$). Based on their measurements in the ducts of different AR values (ranging from 1.0 to 10), they suggested the use of the duct of minimum AR $= 5.0$ in order to avoid three-dimensional (3-D) effect, such that the friction coefficient at the top and bottom walls can be calculated in a relatively precise manner. In order to precisely measure the mean velocity and skin friction coefficient of a two-dimensional (2-D) channel flow, Patel & Head (1969) performed water-channel experiment using a rectangular duct of AR ≈ 48 for different Reynolds numbers. In contrast to these experimental studies of (quasi) 2-D channel flows confined within a rectangular

duct of large AR values, in this research, we aim at studying 3-D rectangular duct flows of relatively low AR values, which feature intense interaction of the four boundary layers developed over the four duct walls.

1.2.3 Computational domain sizes and coherent flow structures

Turbulent flow structures in a duct flow consist of different wavelengths. If the dominant coherent flow structures were not captured in either an experiment or a numerical simulation, the statistical moments (of different orders) of the velocity field would not be correctly calculated. As such, dictated by physics, it is critical to ensure that the streamwise domain size of the duct need to be kept longer than the streamwise wavelengths of dominant eddy motions in DNS. In their pioneering work, Jiménez & Moin (1991) pointed out that there exists a "minimal channel" for DNS of a turbulent plane channel flow. If the computational domain size is smaller than the minimal channel, neither the turbulence level of the flow can be sustained nor turbulence statistics (of different orders) can be correctly predicted. In addition, in order to capture the most energetic eddy motions of the largest scales, a much larger computational domain is typically required in DNS. For instance, to capture elongated near-wall streaky structures in DNS of a turbulent plane channel flow at $Re_\tau = 180$, Del Álamo & Jiménez (2003) kept the streamwise computational domain size at $L_x = 12\pi\delta$ that is three times larger that used in Kim *et al.* (1987).

In fact, the choice of the minimum streamwise computational domain size (L_x) for duct flow is inconsistent. One side supports the use of a relatively short streamwise computational domain of $L_x \leq 8\pi\delta$. Uhlmann *et al.* (2007) and Pinelli *et al.* (2010) conducted a series of DNS studies of square duct flows at Reynolds number $Re_b \leq 3,500$ (based on bulk mean velocity and half duct width). Their streamwise computational domain sizes were set in the range of $0.79\delta \leq L_x \leq 25.13\delta$. Vinuesa *et al.* (2014) conducted DNS of turbulent rectangular duct flows to investigate the aspect ratio effects on turbulence. Their stream-

wise computational domain was kept at $L_x = 25\delta$ for Reynolds numbers of $Re_\tau = 180$ and 330. Yao *et al.* (2015) conducted a LES study of the turbulent square duct flow at $Re_\tau = 300$ — $10,550$ to investigate secondary flows and near-wall turbulence within a streamwise computational domain size of $8\pi\delta$ by following the recommendation of Rhie & Chow (1983). Gavrilakis (1992) performed his DNS study of a turbulent square duct flow with a streamwise domain length of $L_x = 20\pi\delta$. He showed that the predictive accuracy of turbulence statistics is sensitive to the length of streamwise computational domain. Specifically, he observed that the maximum streamwise turbulent intensity predicted based on $L_x = 8\pi\delta$ and $16\pi\delta$ is 6% and 2% lower than that predicted based on $L_x = 20\pi\delta$. Recently, Fang *et al.* (2017) performed DNS of turbulent flow in a spanwise-rotating square duct at $Re_\tau = 150$. In comparison with the DNS results of Dai *et al.* (2015) that were obtained within a small streamwise domain of $L_x = 8\pi\delta$, Fang *et al.* (2017) observed that a substantial fraction of streamwise turbulent kinetic energy could not be captured by using such a small domain.

1.3 Objectives and thesis outline

Thus far, the role of AR in the development of secondary flows and turbulent structures in a rectangular duct has not been well studied in the literature. For instance, due to the interactions of four boundary layers (developed over adjacent sidewalls of different widths under $AR \neq 1$), a proper wall-scaling method is still lacking for establishing a general scale law for the mean velocity. Furthermore, how turbulence statistics vary with the AR value is not yet well understood. In view of this, the current paper aims at investigating the influences of AR value on turbulent flow and structures confined within a rectangular duct of different aspect ratios. Specifically, the AR effects on the formation of secondary flows, velocity scalings, transport of Reynolds stresses, and coherent structures will be studied.

The remaining contents of this paper are arranged as follows. In chapter 2, the nu-

merical algorithm, governing equations, and test cases are introduced. In chapter 3, the numerical results are analyzed to understand turbulence statistics and flow structures. Finally, major conclusions of this research are summarized in chapter 4.

Chapter 2

Test cases and algorithm

Figure 2.1 shows the schematic of the computational domain, coordinate system, and mesh in a quarter of the cross-section of the rectangular duct of AR $= 3.0$. The size of the cross-section of the duct is $L_y = 2\delta$ and $L_z = L_y \times$ AR, where δ denotes the half duct height. No-slip boundary condition is applied to four wall boundaries, the flow field is assumed to be fully developed in the streamwise direction. The Reynolds number is fixed at $Re_\tau = u_\tau \delta/\nu \approx 150$, where u_τ and ν denotes the wall-friction velocity and kinematic viscosity, respectively. For DNS of an incompressible flow, the governing equations are written as follows:

$$\begin{aligned} &\frac{\partial u_i}{\partial x_i} = 0\,, \\ &\frac{\partial u_i}{\partial t} + u_j \frac{\partial u_i}{\partial x_j} = -\frac{1}{\rho}\frac{\partial p}{\partial x_i} + \nu \frac{\partial^2 u_i}{\partial x_j \partial x_j} - \frac{\Pi}{\rho}\delta_{1i}\,. \end{aligned} \tag{2.1}$$

where u_i (with $i = 1$, 2 and 3) denote velocity components in the streamwise (x_1 or x), vertical (x_2 or y) and spanwise (x_3 or z) directions, respectively, p is the pressure, and Π denotes the constant mean pressure gradient along streamwise direction. Also, δ_{ij} and ρ represent the Kronecker delta and density of the fluid, respectively.

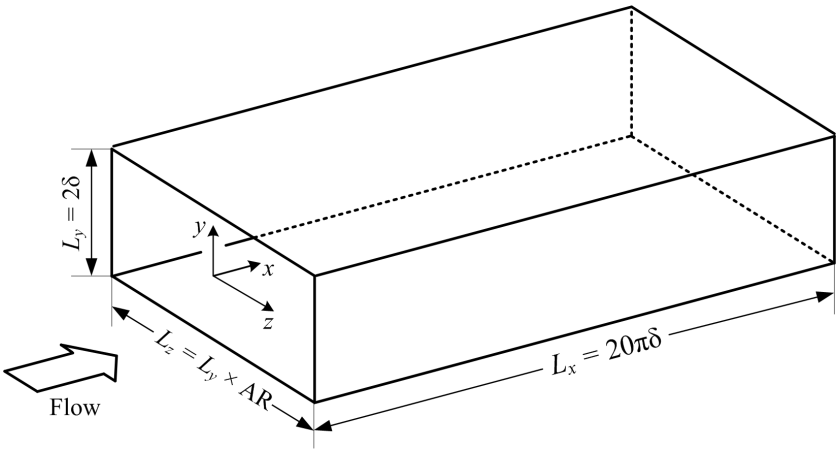

(a) Computational domain

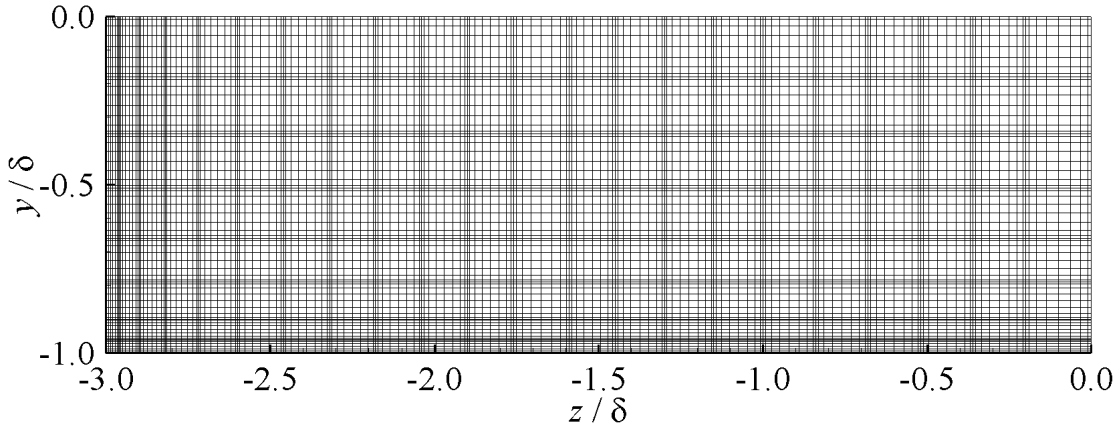

(b) Grids in a quadrant of cross section

Figure 2.1: Computational domain, coordinate system and grids in a quarter of the cross-section of the rectangular duct of AR $= 3.0$.

The current DNS study is performed using “Semtex", an open-source spectral-element code publicly shared by Blackburn & Shewin (2004). This code is written with programming languages C++ and FORTRAN. More specifically, the main computing cores, such as matrix multiplication, are implemented and vectorized using FORTRAN, whereas C++ is employed for developing scripts for post-processing of data using an object-oriented programming approach. Fourier series and quadrilateral spectral elements are used to express all the variables (velocity, pressure and all the other indeterminate variables) in the stream-

Table 2.1: Summary of test cases, grid sizes and sampling times.

Duct Case	Re_b	$L_x \times L_y \times L_z$	$N_x \times N_y \times N_z$	LETOTs
AR1P0	2222	$20\pi\delta \times 2\delta \times 2\delta$	$960 \times 129 \times 129$	41
AR1P5	2274	$20\pi\delta \times 2\delta \times 3\delta$	$960 \times 129 \times 193$	61
AR2P0	2290	$20\pi\delta \times 2\delta \times 4\delta$	$960 \times 129 \times 241$	61
AR2P5	2331	$20\pi\delta \times 2\delta \times 5\delta$	$960 \times 129 \times 321$	95
AR3P0	2327	$20\pi\delta \times 2\delta \times 6\delta$	$960 \times 129 \times 289$	102
AR3P0a	2334	$2\pi\delta \times 2\delta \times 6\delta$	$96 \times 129 \times 289$	41
AR3P0b	2308	$4\pi\delta \times 2\delta \times 6\delta$	$192 \times 129 \times 289$	41
AR3P0c	2362	$8\pi\delta \times 2\delta \times 6\delta$	$384 \times 129 \times 289$	41

wise direction and cross-stream planes, respectively (Karnizdakis & Shewin, 2005). This code is parallelized following the message passing interface (MPI) standard. The high-order time splitting scheme proposed by Karnizdakis *et al.* (1991) is employed for the time integration. Specifically, following the backward-time differencing scheme, intermediate velocity fields are obtained in the first sub-step by advecting convection and body force (Π) terms. In the second and last sub-steps, the pressure and viscous corrections are obtained to enforce the incompressibility, respectively. In addition, a direct solver is employed to solve the Helmholtz equation for each wavenumber following the Galerkin projection. At each time step, the pressure gradient is adjusted to maintain a fixed bulk mean velocity, $U_b = 1.0$.

In total, 960 equally spaced grids are used along the streamwise direction, i.e., 480 wavenumbers are adopted in the Fourier space. For all simulations, the streamwise spacing is maintained at $\Delta\, x^+ = 9.82$. For each rectangular element in the cross stream plane, an eighth-order Gauss-Lobatto-Legendre (GLL) Lagrange shape function is used for spatial interpolation in each direction. More elements were used in the spanwise direction of the duct of higher AR values. The grids spacing in the cross-stream plane is refined in the near-wall region and stretched in the duct center, and in wall units, varies as $\Delta\, y^+ \in [0.3, 4.9]$ and $\Delta\, z^+ \in [0.3, 5.45]$. The time step is fixed at $\Delta\, tU_b/\delta = 2 \times 10^{-3}$, and correspondingly, the Courant-Friedrichs-Lewy (CFL) number is kept lower than 0.3. Table. 2.1 summarizes

the test cases, the grids sizes, and the large eddy-turnover times (LETOTs $= tu_\tau/\delta$, where t represents the total flow time) employed in this DNS study. In the case names shown in Table 2.1, "AR" stands for aspect ratio, "P" is the initial letter for "point", and the last affixed letters "a", "b", and "c" is used to indicate the streamwise domain lengths of $L_x = 2\pi\delta$, $4\pi\delta$, and $8\pi\delta$, respectively. For example, case "AR3P0b" represents a computational domain of AR $= 3.0$ and $L_x = 8\pi\delta$.

Chapter 3

Results and discussions

In this chapter, turbulence statistics will be analyzed in details. Specifically, the streamwise computational domain size will be first determined in order to ensure the predictive accuracy of turbulence statistics. Then, a detailed analysis of influences of the secondary flows on turbulence statistics will be provided. Then, the budget balance of Reynolds stresses and the wall scaling method will be studied. Finally, turbulent flow structures in the duct of higher aspect ratios will be investigated.

3.1 Computational domain

In a rectangular duct, energy-containing flow structures are elongated in the streamwise direction. In order to accurately predict statistical moments of the velocity field, the streamwise computational domain size must be kept sufficiently large such that all dominant coherent flow structures may fully evolve in the streamwise direction and their wavelengths can be captured in a numerical simulation. To this purpose , cases “AR3P0a", “AR3P0b", “AR3P0c", and “AR3P0" are designed to determine the minimum streamwise domain size for performing DNS of the rectangular duct flow of AR $= 3.0$. The reason that case AR3P0

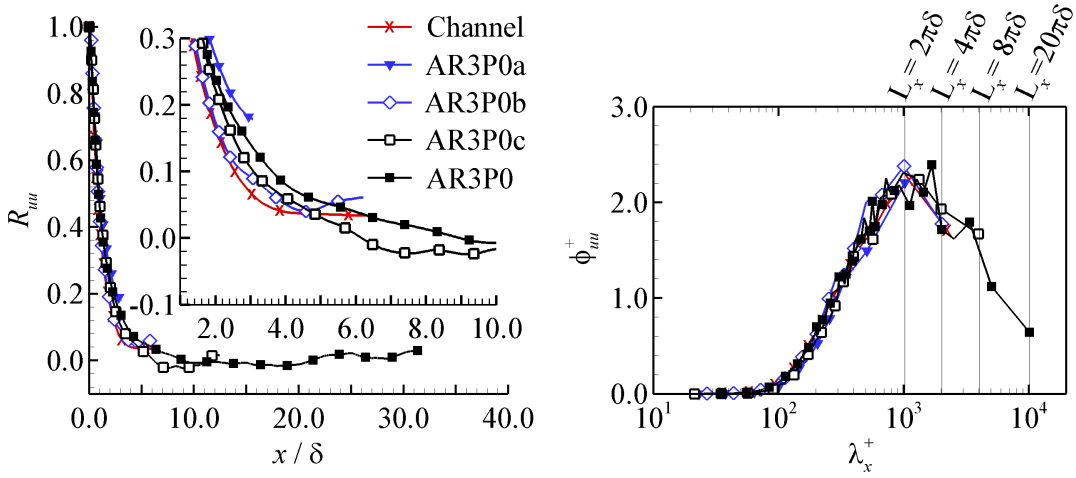

(a) Two point autocorrelation (b) Pre-multiplied energy spectra

Figure 3.1: The two-point velocity autocorrelations and one-dimensional (1-D) pre-multiply energy spectra along streamwise direction at the coordinate $y^+ \approx 11.8$ for cases AR3P0a, AR3P0b, AR3P0c, and AR3P0. The four vertical lines demarcate the streamwise boundaries of these four test cases (of different streamwise domain sizes $L_x = 2\pi\delta$, $4\pi\delta$, $8\pi\delta$, and $20\pi\delta$, respectively). For the purpose of comparison, the plane channel flow results of Kim *et al.* (1987) are also presented in the figure.

is selected is that it has the longest streamwise domain size (of $L_x = 20\pi\delta$), which facilitates the comparative study by providing an accurate prediction of the streamwsie turbulent flow structures (which become increasingly elongated as the AR value increases).

In the literature, the streamwise two-point autocorrelation R_{uu} is commonly used for determining whether the streamwise computational domain size is sufficiently long, being able to capture streamwise-correlated energetic flow structures. However, Gavrilakis (1992) argued that the use of two-point autocorrelations is “unsafe". Fig. 3.1 shows the results of two-point velocity autocorrelations R_{uu} and pre-multiplied 1-D energy spectra ϕ^+_{uu} at $y^+ \approx 11.8$. In the figure, λ^+_x represents the streamwise wavelength ($\lambda_x = 2\pi/k_x$) non-dimensionalized by the wall unit, i.e., $\lambda^+_x = (\lambda_x u_\tau)/\nu$. Here, k_x is the streamwise wavenumber. In order to facilitate the comparison, the streamwise domain sizes of test cases (for $L_x = 2\pi\delta$, $4\pi\delta$, $8\pi\delta$ and $20\pi\delta$) are labeled using vertical lines. As seen in

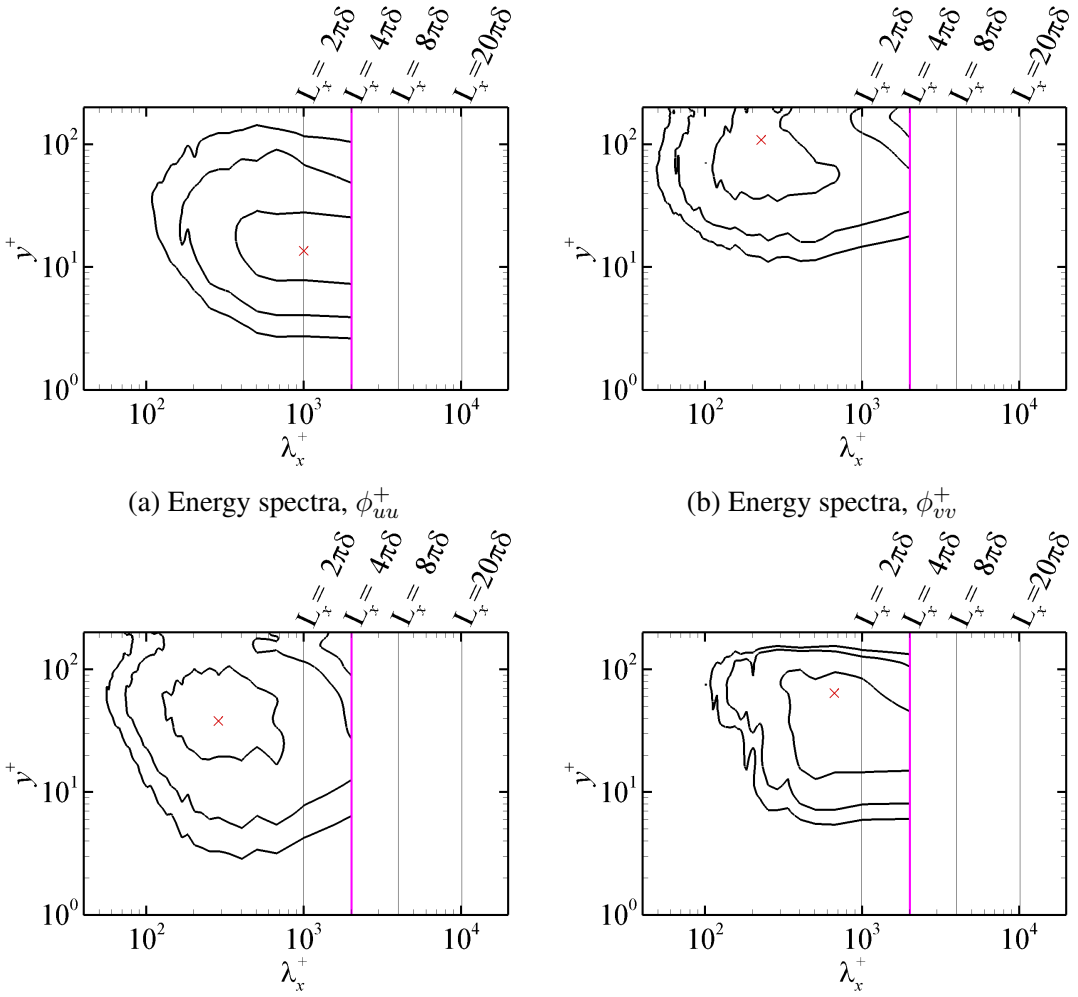

(a) Energy spectra, ϕ_{uu}^+

(b) Energy spectra, ϕ_{vv}^+

(c) Energy spectra, ϕ_{ww}^+

(d) Energy co-spectra, $-\phi_{uv}^+$

Figure 3.2: Isopleths of streamwise pre-multiplied 1-D energy spectra and co-spectra w.r.t. the streamwise wavelength, λ_x^+ in the central vertical plane (at $z/\delta = 0.0$) for case AR3P0b. The symbols "$\times$" marks the location of peak value of energy spectra. Three contour levels shown in the figure panels are at 62.5%, 25% and 12.5% of the peak value. The four vertical lines demarcate the streamwise domain boundaries of $L_x = 2\pi\delta$, $4\pi\delta$, $8\pi\delta$, and $20\pi\delta$.

Fig. 3.1(a), the streamwise two-point autocorrelations decay approximately to zero at $x/\delta > 4$, except for the case AR3P0a. From Fig. 3.1(b), it is apparent that ϕ_{uu}^+ peaks around $\lambda_x^+ \approx 10^3$, a coordinate value that was also reported by Jiménez (1998). More importantly, Fig. 3.1(b) shows that in the channel case, and duct cases AR3P0b and AR3P0c,

the streamwise energy only decays to about 77%, 75% and 72% of their peak values, respectively. This indicates that there is a substantial fraction of energy missed by DNS due to the use of a small computational domain size, a conclusion that is consistent with the observation of Fang *et al.* (2017) who studied the effect of streamwise domain size on the predictive accuracy of DNS of a square duct flow. In contrast, the streamwise energy in the case AR3P0 only misses 25% of its maximum, indicating that most energy-containing eddy motions have been well captured by current DNS.

Figs. 3.2 and 3.3 show the pre-multiplied 1-D energy spectra and co-spectra at different elevations (or of different y^+ values) in the central vertical plane (at $z/\delta = 0.0$) of duct cases AR3P0b and AR3P0. The contour levels of energy spectra are 62.5%, 25% and 12.5% of the peak value, and the peak locations are marked using symbol "$\times$" in the figure. Following Hoyas & Jiménez (2006), two threshold values of 62.5% and 12.5% of the maximum energy are used to identify the "most energetic core" and "active range" of eddy motions (or, the "inner" and "outer" bounds of energetic eddies). However, to fully capture the outer bound of energetic eddies requires an enormous computing time. Therefore, the current streamwise computational domain size aims at fully capturing the contour corresponding to 25% of the energy peak value instead, namely, the "intermediate" bound of eddies. As seen in the Fig. 3.2, it is apparent that the streamwise domain size of $L_x = 4\pi\delta$ is definitely insufficient because all bounds of energetic eddies were chopped-off abruptly at the wavelength that equals to the streamwise domain size, except for the inner bounds of eddies of ϕ^+_{vv} and ϕ^+_{ww}. This indicates a significant amount of energy is missing due to the use of an overly short streamwise computational domain size. In comparison, as shown in the Fig. 3.3, it is apparent that most of inner and intermediate bounds of energetic eddies and co-spectra are very well captured within the streamwise domain size of $L_x = 20\pi\delta$ (only 1.9% of streamwise TKE is missed by the intermediate bounds of ϕ^+_{uu} as shown in Fig. 3.3(a)). In particular, Figs. 3.3(b)-(c) show that the inner, intermediate, and even the outer ranges of eddy motions as indicated by pre-multiplied 1-D energy spectra ϕ^+_{vv} and

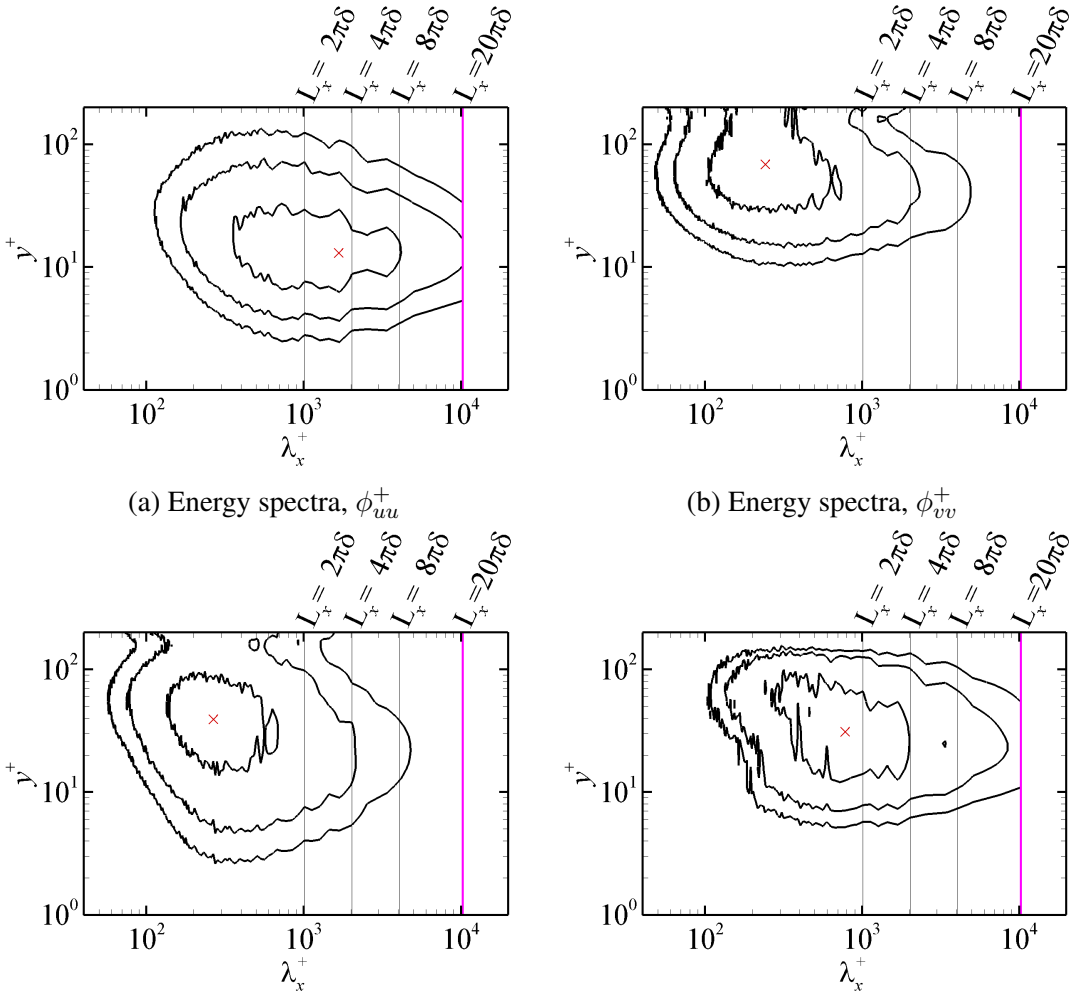

(a) Energy spectra, ϕ^+_{uu}

(b) Energy spectra, ϕ^+_{vv}

(c) Energy spectra, ϕ^+_{ww}

(d) Energy co-spectra, $-\phi^+_{uv}$

Figure 3.3: Isopleths of streamwise pre-multiplied 1-D energy spectra and co-spectra w.r.t. the streamwise wavelength, λ^+_x in the central vertical plane (at $z/\delta = 0.0$) for case AR3P0. The symbols "$\times$" marks the location of peak value of energy spectra. Three contour levels shown in the figure panels are at 62.5%, 25% and 12.5% of the peak value. The four vertical lines demarcate the streamwise domain boundaries of $L_x = 2\pi\delta$, $4\pi\delta$, $8\pi\delta$, and $20\pi\delta$.

ϕ^+_{ww} have been completely captured using the large streamwise domain size of $L_x = 20\pi\delta$. Furthermore, by comparing Figs. 3.2(d) and 3.3(d), it is found that the peak position of pre-multiplied 1-D co-spectra moves towards longer wavelength as the value of L_x increases. For instance, the energy co-spectra $-\phi^+_{uv}$ predicted based on a small streamwise domain

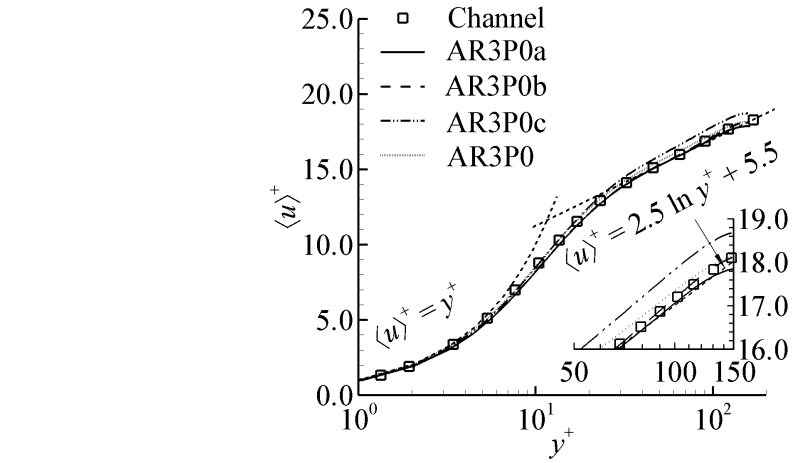

(a) Mean streamwise velocity

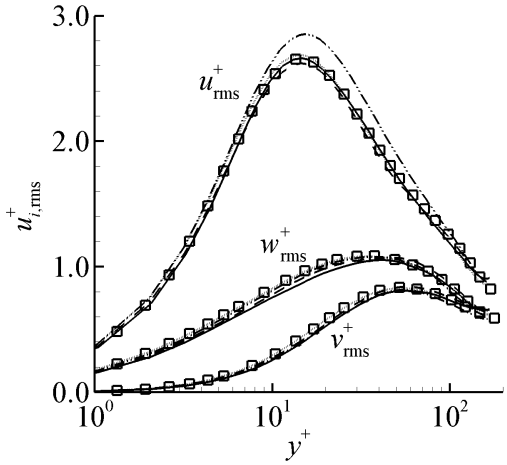

(b) RMS velocities

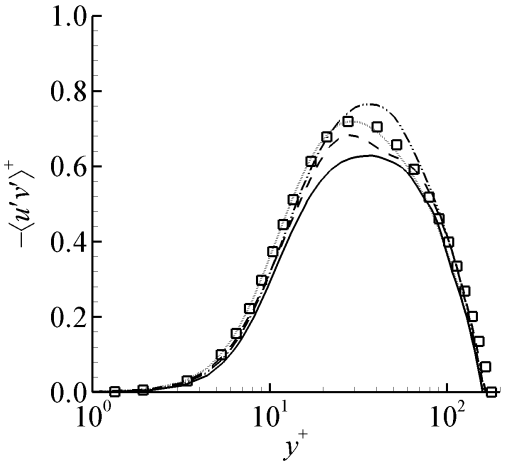

(c) Reynolds shear stress

Figure 3.4: Non-dimensionalized mean streamwise velocity, RMS of velocity fluctuations, and Reynolds shear stresses at the central vertical plane (at $z/\delta = 0.0$) of duct cases AR3P0a, AR3P0b, AR3P0c, and AR3P0. For the purpose of comparison, the plane channel flow data of Kim *et al.* (1987) are also shown in the figure.

size of $4\pi\delta$ peaks around $\lambda_x^+ \approx 670$, but at $\lambda_x^+ \approx 780$ based on a longer streamwise size of $20\pi\delta$. This clearly indicates that the characteristic streamwise wavelength of energetic eddy motions (as indicated by the peak of the energy spectra or co-spectra) can be artificially shortened by the use of small computational domain sizes, an erroneous condition that should be avoided in a DNS. To further examine the significance of the streamwise

computational domain size, on the statistical results of the velocity field, Fig. 3.4 compares the mean streamwise velocity, root mean square (RMS) velocities, and Reynolds shear stresses at the central vertical plane (at $z/\delta = 0.0$) of duct cases AR3P0a, AR3P0b, AR3P0c, and AR3P0. For the purpose of comparison, the plane channel flow data of Kim *et al.* (1987) are also shown in the figure. From Fig. 3.4, it is apparent that the trends of the profiles of the first- and second-order flow statistics do not vary monotonically with the value of the streamwise domain size L_x. Among the four test cases of different duct lengths, the discrepancy in turbulence statistics at the duct center (at $z/\delta = 0.0$) between case AR3P0 and the plane channel flow case of Kim *et al.* (1987) is the minimum. Specifically, the RMS value from case AR3P0 peaks at $y^+ \approx 13.5$, which is within 1% difference with the channel flow result. Furthermore, as is evident in the Fig. 3.4(c), the profile of the Reynolds shear stress from the plane channel flow case only collapses with that of case AR3P0.

Based on the above analysis of the pre-multiplied 1-D energy spectra and co-spectra, and the first- and second-order flow statistics, we conclude that a minimal streamwise domain size of $L_x = 20\pi\delta$ is needed for conducting accurate DNS study of rectangular duct flows. The conclusion is consistent with those of Gavrilakis (1992) and Fang *et al.* (2017), who performed DNS studies of studies of turbulent flows confined within stationary and rotating square ducts, respectively. In view of this, the DNS results presented in the remainder of this paper are based on the largest streamwise computational domain size of $L_x = 20\pi\delta$.

3.2 Mean and secondary flows

Flows within closed rectangular ducts feature secondary flows, and it is of interest to investigate how the mean and secondary flows are influenced by the AR values and the four boundary layers developed over the four walls. Fig. 3.5 compares the mean and cross-

stream velocity contours in the cross-section (y-z plane) of rectangular ducts of different AR values. In the figure, the magnitude of the mean cross-stream velocity $\langle u_{\text{cs}} \rangle$ is calculated as $\langle u_{\text{cs}} \rangle = \sqrt{\langle v \rangle^2 + \langle w \rangle^2}$ to quantify the magnitude of cross stream velocity. Note that in Fig. 3.5, no enforcement of symmetry is applied because of an extremely long time durations was used for calculating flow statistics to ensure achieving the natural convergence of mean secondary flows and geometrical symmetry. For instance, in cases AR1P0 and AR3P0, the LETOTs were maintained at 41 and 102, respectively, which is significant larger than that used in the literatures (Fang *et al.*, 2017; Gavrilakis, 1992; Vinuesa *et al.*, 2014). From the left-hand side of Fig. 3.5, the secondary flows of Prandtl's second kind appear as one pair of counter-rotating vortices residing in each corner of the cross-stream plane. Particularly, it is observed that the streamwise mean secondary flow vortices are symmetrical about the diagonal line in the square duct (case AR1P0), but non-symmetrical in the other four rectangular duct cases (for AR $= 1.5$, 2.0, 2.5 and 3.0). Furthermore, as the AR value increases, it is apparent in the figure that the vortices near the top and bottom walls (at $y/\delta = \pm 1.0$) grow in size and extend towards the duct center, an observation that is consistent with the findings of Vinuesa *et al.* (2014).

The AR effect on the strength of the cross-stream velocity $\langle u_{\text{cs}} \rangle^+$ can be seen by comparing the right-half figure panels of the five cases (of AR $= 0$, 1.5, 2.0, 2.5 and 3.0). It is observed that the maximum value of $\langle u_{\text{cs}} \rangle^+$ of case AR3P0 significantly increases by 21% compared to that in the square duct case AR1P0 (i.e., as the AR value increases from 1.0 to 3.0). The value of $\langle u_{\text{cs}} \rangle^+$ peaks around $(y^+, z^+) = (12, 69)$ for all test cases, a result that is consistent with the report of Gavrilakis (1992). From the figure legends, it is clear that the magnitude of the cross-stream velocity $\langle u_{\text{cs}} \rangle^+$ is two orders smaller than that of the mean streamwise velocity $\langle u_{\text{cs}} \rangle^+$. Furthermore, near the vertical central plane (at $z/\delta = 0.0$) of the duct, the value of $\langle u_{\text{cs}} \rangle^+$ is trivially small. As a result, it is expected the behaviour of a rectangular duct flow to be close to a Poiseuille plane channel flow (near the vertical center plane), especially at high AR values. Furthermore, it is clear from the figure that the width

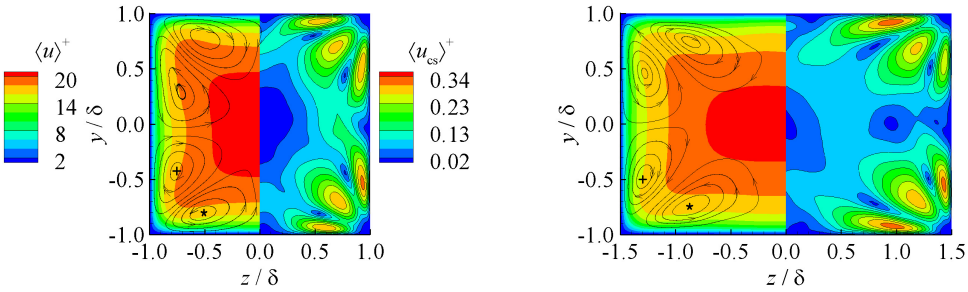

(a) Case AR1P0 (b) Case AR1P5

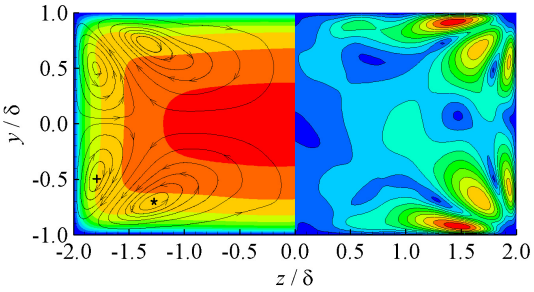

(c) Case AR2P0

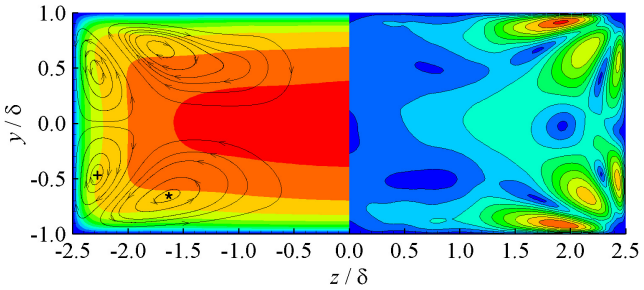

(d) Case AR2P5

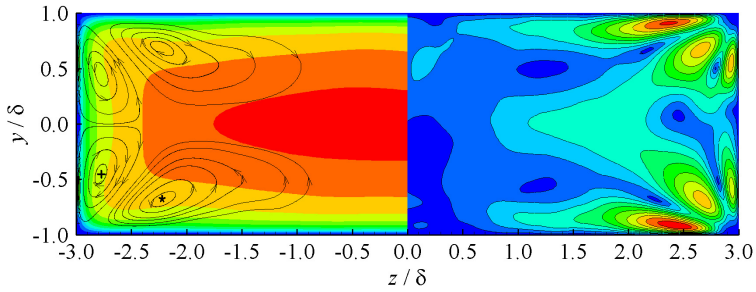

(e) Case AR3P0

Figure 3.5: Mean secondary flows in the y-z plane of rectangular ducts of different AR values (varying from 1.0 to 3.0). The left-half figure panel shows the contours of the mean streamwise velocity ($\langle u \rangle^+$) superimposed with streamlines of the mean cross-stream velocity vector ($\langle v \rangle, \langle w \rangle$) and the right-half figure panel shows the contours of the mean cross-stream velocity ($\langle u_{cs} \rangle^+$). The vortex cores of the mean secondary flow are marked using symbol legends "+" and "⋆".

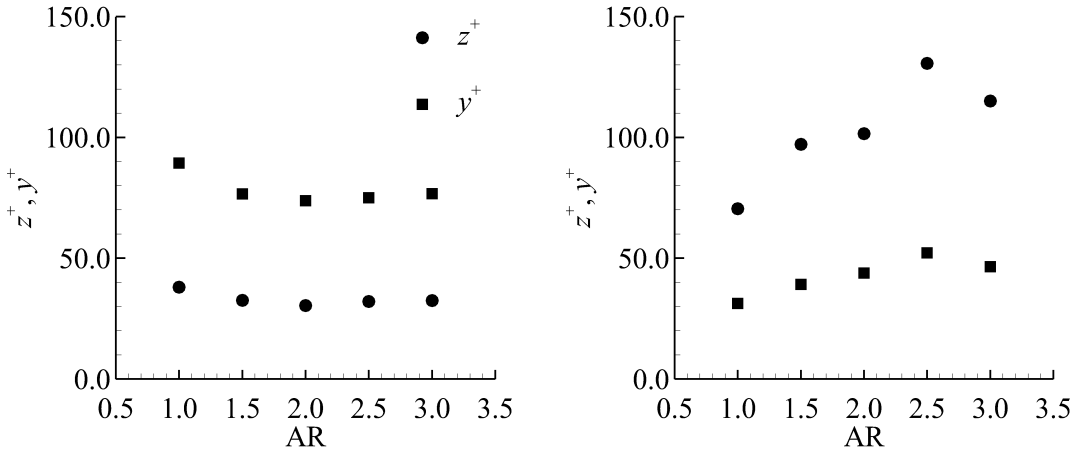

(a) Positions of vertical sidewall vortex core (b) Positions of bottomwall vortex core

Figure 3.6: The position of vortex core in wall coordinates as a function of the AR value. The distances to side and bottom walls are non-dimensionalized by local friction velocity $u_{\tau,\text{local}}$. The position of the vortex cores are in Fig. 3.5.

of Poiseuille-like flow region increases in the spanwise direction as AR increases.

Now, the research can be refined by investigating the movement of vortex cores of secondary flows in response to an increasing AR value. Following Vinuesa *et al.* (2014), the vortex cores are detected using the local minima of $\langle u_{\text{cs}} \rangle^+$. In each corner, there are a pair of vortex cores, one close to the horizontal bottom (or top) wall, and the other close to the vertical sidewall. Given the vertical symmetry of the domain, only one pair of vortex cores are shown in the Fig. 3.5, marked using symbols "**+**" and "**⋆**" . Fig. 3.6 shows the positions of vortex cores in coordinates of y^+ and z^+. As seen in the Fig. 3.6(a), although the value of y^+ and z^+ are slightly higher at for the square duct case (of AR $= 1.0$), the positions of vortex core near the vertical sidewall are stable, as the coordinates are constantly around (y^+, z^+) $\approx$ (75, 35) with an varying AR value. This indicates that the position of the sidewall vortex core is independent of the AR values larger than 1.0. In contrast, as shown in Fig. 3.6(b), the bottom vortex core first moves away from the bottom wall as AR increases from 1.0 to 2.5, and then, it slightly returns to the bottom wall as AR

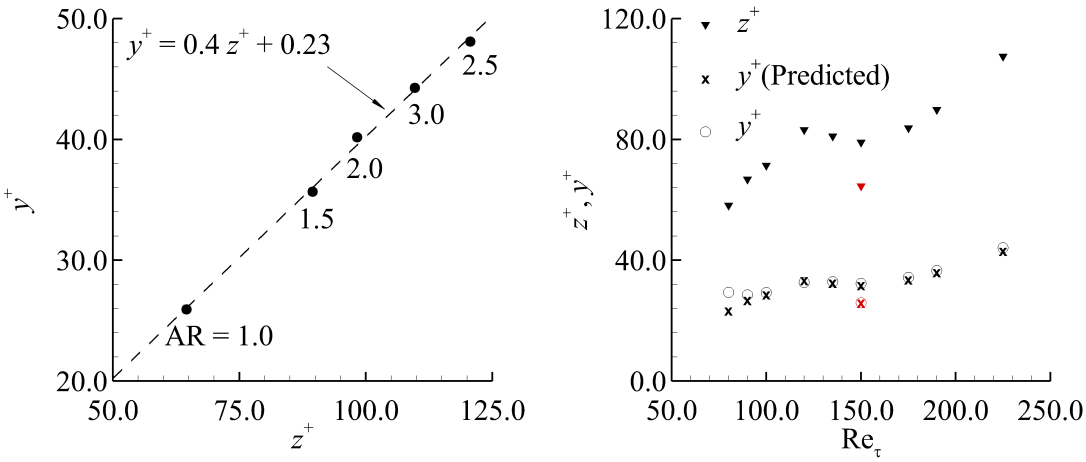

(a) Position of the bottomwall vortex core at different AR values

(b) Position of the bottomwall vortex core at different Reynolds numbers

Figure 3.7: Positions of the bottomwall vortex core at different AR values and Reynolds numbers. Note that in panel (b), symbols ▼ and ○ represent the positions of vortex cores captured using the maximum mean cross-streamline function, $\langle\psi(y,z)\rangle$ of Pinelli *et al.* (2010), and symbol $\times$ denotes the predicted value of y^+ using Eqn. (3.1), i.e., the trend-line function shown in panel (a). The current results of square duct flow at $Re_\tau = 150$ shown in panel (b) are indicated in red color.

reaches 3.0. Specifically, the bottom vortex core first moves from $(y^+,\, z^+) \approx (30, 75)$ to $(50, 120)$ as the AR value increases from 1.0 to 2.5, and then it drops slightly to $(45, 110)$ as the AR value continues to increase from 2.5 to 3.0.

Figure 3.7 shows how the position of the bottomwall vortex core varies with the AR value and Reynolds numbers. From Fig. 3.7(a), it is very interesting to observe the scatter plots of the positions of the bottomwall vortex cores at different AR values show a clear linear pattern. Furthermore, through a least-squares regression analysis, the wall coordinates of the bottom vortex core can be further fitted to a linear function as

$$y^+ = 0.4z^+ + 0.23, \quad \text{for AR} \in [1.0, 3.0]. \tag{3.1}$$

The linear relationship holds strongly within the range of the AR values tested, as a maxi-

mum offset error of 1.65% (of in case AR2P0) with the sum of squares of vertical deviation of 0.9975. In order to verify this linear relationship, the current study compared the presenting results with DNS results of Pinelli *et al.* (2010) as shown in Fig. 3.7(b). In the DNS of turbulent square duct flows, Pinelli *et al.* (2010) define the vortex cores using the maximum streamline function $\langle\psi(x,y)\rangle$ in order to investigate Reynolds number effects on the secondary flows. From Fig. 3.7(b), it is apparent that as Reynolds number becomes larger enough, i.e., $Re_\tau \geq 100$, the predicted y^+ ($\times$) and the actual y^+ ($\circ$) extracted from DNS result of Pinelli *et al.* (2010) are in an excellent agreement. This shows our linear function of the position of bottom vortex core is valid for both different AR and Reynolds number simulations. Base on the result, we conclude that in the rectangular ducts of small AR values (of AR ≤ 3.0) at $Re_\tau \geq 100$, the positions of bottom vortex core are independent from varying AR values.

3.3 Turbulent Statistics

Due to the interactions between boundary layers developed over the four walls, there is an ambiguity in choosing a proper velocity scaling from either the average friction velocity $u_{\tau,\,\mathrm{avg}}$ or the local friction velocity $u_{\tau,\,\mathrm{local}}$ in the non-dimensionalization of the mean streamwise velocity as in the derivation of the classical law-of-the-wall. To decide, the current study tried both these velocity scalings to non-dimensionalize the mean streamwise velocity in the central vertical plane (at $z/\delta = 0.0$) and the central horizontal plane (at $y/\delta = 0.0$) of a rectangular duct. Figure 3.8 shows the semi-logarithmic plot of the mean streamwise velocity $\langle u\rangle^+$ in the wall coordinates for all test cases. Figures 3.8(a)-(b) show the mean streamwise velocities non-dimensionalized by the averaged friction velocity ($u_{\tau,\,\mathrm{avg}}$) and the local friction velocity ($u_{\tau,\,\mathrm{local}}$), respectively. While in the Figs. 3.8(c)-(d), the mean streamwise velocity in the central horizontal plane (at $y/\delta = 0.0$) is plotted, non-dimensionalized by these two different wall friction velocities $u_{\tau,\,\mathrm{avg}}$ and $u_{\tau,\,\mathrm{local}}$, re-

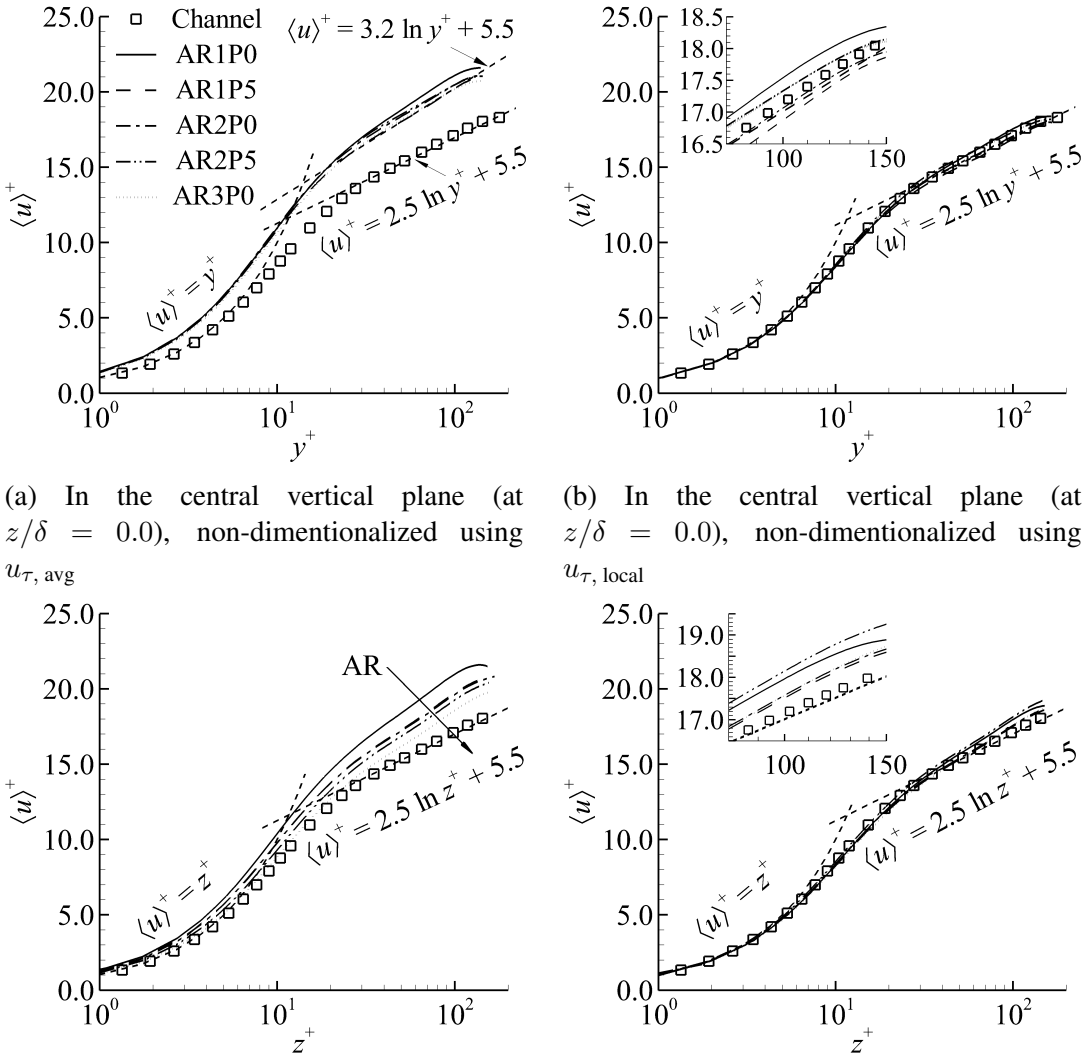

(a) In the central vertical plane (at $z/\delta = 0.0$), non-dimentionalized using $u_{\tau,\,\mathrm{avg}}$

(b) In the central vertical plane (at $z/\delta = 0.0$), non-dimentionalized using $u_{\tau,\,\mathrm{local}}$

(c) In the central horizontal plane (at $y/\delta = 0.0$), non-dimentionalized using $u_{\tau,\,\mathrm{avg}}$

(d) In the central horizontal plane (at $y/\delta = 0.0$), non-dimentionalized using $u_{\tau,\,\mathrm{local}}$

Figure 3.8: Mean streamwise velocity profile in the central vertical plane (at $z/\delta = 0.0$) and the central horizontal plane (at $y/\delta = 0.0$). Note that for the purpose of comparison, the plane channel data of Kim *et al.* (1987) are also presented. The arrow in panel (c) points to the direction of an increasing AR value.

spectively. For the purpose of the comparison, the plane channel flow data of Kim *et al.* (1987) (indicated as symbol squares in the figure) and the universal linear and logarithmic

laws-of-the-wall for a zero-pressure-gradient (ZPG) boundary layer are also presented in the figures. From Fig. 3.8(a), it is apparent that the streamwise velocity profiles in the the central vertical plane (at $z/\delta = 0.0$) of the rectangular ducts of different AR values deviate significantly from the channel flow results of Kim *et al.* (1987) and the conventional Kármán's two-layer model for the law-of-the-wall. As seen in the viscous sublayer, the mean streamwise velocities from testing cases are significantly larger than that of the channel flow, which implies a larger velocity gradient and a concomitant larger wall friction stress. Away from the wall, the logarithmic scaling yields

$$\langle u \rangle^+ = 3.2 \ln\, y^+ + 5.5 \tag{3.2}$$

where the slope is 3.2, a result that is consistent with that of Gavrilakis (1992) for DNS of a square duct flow. From Fig. 3.8(c), it is apparent that the mean streamwise velocity profiles in the central horizontal plane (at $y/\delta = 0.0$) of the rectangular ducts becomes increasingly similar to that characteristic of a 2-D ZPG boundary layer as AR increases. Nevertheless, it is interesting to see from Figs. 3.8(b) and 3.8(d) once the mean streamwise velocity profile is rescaled using $u_{\tau,\,\text{local}}$, the overall agreement is dramatically improved. In particular, as a direct result of using local wall friction velocity, the agreement is excellent in the viscous sublayer. In view of this, we concluded that the use of local friction velocity is indeed necessary in order to obtain an universal law-of-the-wall in a rectangular duct flow, a conclusion that is similar to those of Gavrilakis (1992) and Vinuesa *et al.* (2014). As a result, the local friction velocity $u_{\tau,\,\text{local}}$ is used for the non-dimensionalizations of quantities that are expressed using units in the remainder of this thesis.

Figure 3.9 shows the distribution of non-dimensional TKE in the cross-stream (y-z) plane with different AR values, where TKE is defined as $k = \langle u_i' u_i' \rangle / 2$ with $i = 1$, 2, and 3. The time-averaged vector field shown in the figure consists of the vertical and spanwise velocities v'^+ and w'^+, which are displayed at every 4 vertical and spanwise grid points in

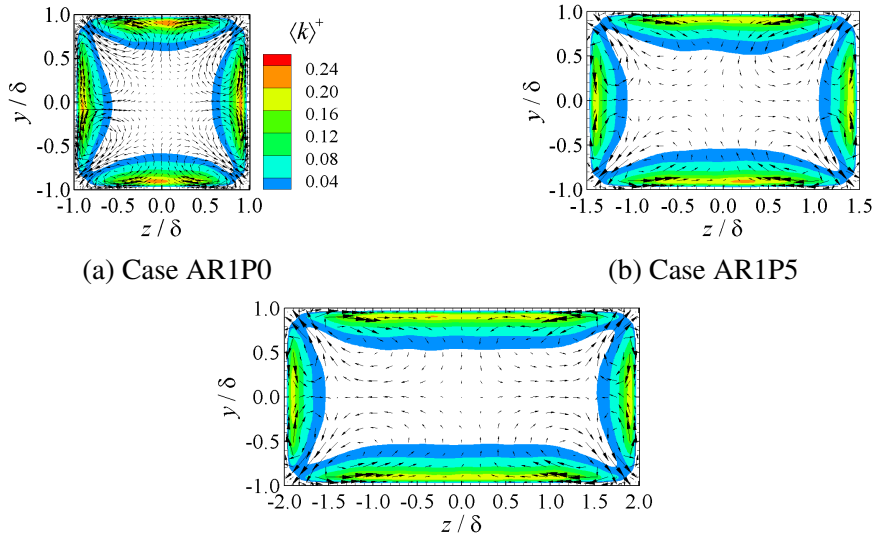

(a) Case AR1P0

(b) Case AR1P5

(c) Case AR2P0

(d) Case AR2P5

(e) Case AR3P0

Figure 3.9: Contours of TKE k (non-dimensionalized by u_τ^2) in the cross-stream (y-z) plane at different AR values. The time-averaged vector field shown in the figure consists of the vertical and spanwise velocities v^+ and w^+, which are displayed at every 4 vertical and spanwise grid points in panel (a), and at every 8 vertical and spanwise grid points for clear views of both vector field and secondary flow structures. Note that contours corresponding to low TKE levels (less than 10% of peak value) are chopped off for a clear view of TKE distributions.

Fig. 3.9(a), and at every 8 vertical and spanwise grid points for clear views of both vector field and secondary flow structures. Note that contours corresponding to low TKE levels (less than 10% of peak value) are chopped off for a clear view of TKE distributions. From Fig. 3.9, it is apparent the TKE distribution exhibits an interesting 4-point-star pattern. This is due to the restriction from the duct walls and the secondary flow pattern discussed above. In the corner regions (at $z^+ \approx 45$), as the major contributor to the streamwise TKE, the streamwise production is dramatically reduced due to the interactions of two interested walls (top/bottom and side walls) (Vinuesa *et al.*, 2014). Consequently, the magnitude of TKE along the wall bisector is much reduced (below 20% of k^+_{max}). Interestingly, it is also found that the value of corner TKE is maintained constantly at 0.04 as AR increases, implying that the corner TKE level is independent from AR, as the flow physics are dominated by the two adjacent walls in the corner. Moreover, contours corresponding to high TKE (larger than 83% of k^+_{max}) are found identically at near-wall centre regions, located at $y^+ \approx 15$ and $z^+ \approx 15$ away from corners. This near-wall location corresponds to the positions of maximum production, i.e., $-\langle u'v'\rangle \partial\langle u\rangle/\partial y$ and the secondary flow velocities (Kim *et al.*, 1987; Gavrilakis, 1992).

Figure 3.10 shows the root-mean-square (RMS) velocities and the Reynolds shear stresses in the central vertical plane (at $z/\delta = 0.0$) and the central horizontal plane (at $y/\delta = 0.0$). As seen in Fig. 3.10(a), in the central vertical plane, the streamwise RMS velocities for larger AR ducts (i.e., in cases AR2P0, AR2P5 and AR3P0) are in a very good agreement with the channel flow result. However, those for smaller AR ducts (i.e., in cases AR1P0 and AR1P5) are slightly over-predicted. In fact, as AR becomes greater than 2.0, the difference in the magnitude of u^+_{rms} between the test cases and the plane channel flow of Kim *et al.* (1987) is less then 1%, indicating that the near wall-behaviour of u^+_{rms} recovers that characteristic of a 2-D ZPG boundary-layer flow. It is also apparent in the figure that the vertical and spanwise RMS velocity components are in an excellent agreement with that in the channel flow for all AR values tested. From Fig. 3.10(b), it is apparent that similar to

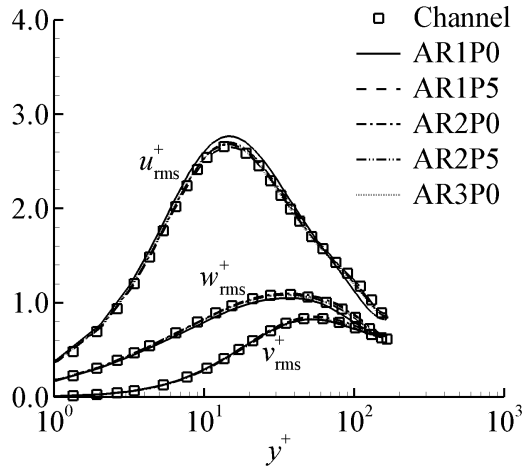

(a) RMS velocities displayed in the central vertical plane (at $z/\delta = 0.0$).

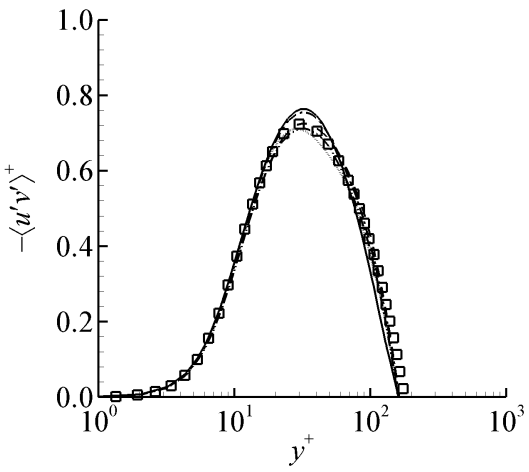

(b) Reynolds shear stress $-\langle u'v' \rangle^+$ displayed in the central vertical plane (at $z/\delta = 0.0$).

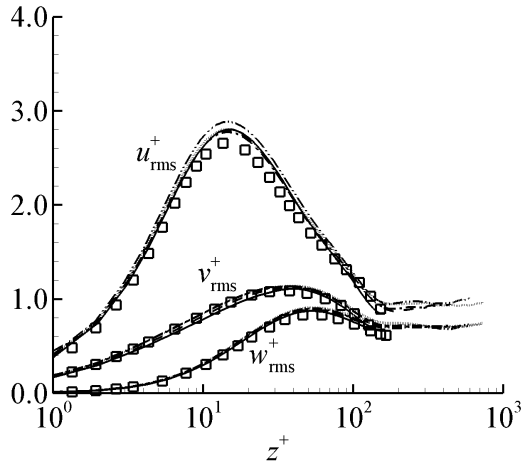

(c) RMS velocities displayed in the central horizontal plane (at $y/\delta = 0.0$).

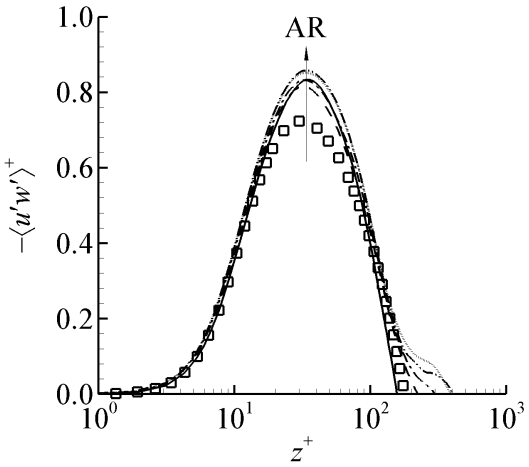

(d) Reynolds shear stress $-\langle u'w' \rangle^+$ displayed in the central horizontal plane (at $y/\delta = 0.0$).

Figure 3.10: Profiles of non-dimensionalized RMS velocities and Reynolds shear stresses in the central vertical plane (at $z/\delta = 0.0$) and the central horizontal plane (at $y/\delta = 0.0$). Note that for the purpose of comparison, the plane channel flow data of Kim *et al.* (1987) are also presented. The arrow in panel (d) points to the direction of an increasing AR value.

the behavior of streamwise RMS velocity, the profile of Reynolds shear stress $-\langle u'v' \rangle$ in the ducts of high AR values (of AR ≥ 2.0) collapses well. Precisely, at $y^+ = 30$, the dif-

ference in the peak value of Reynolds shear stress between the plane channel flow of Kim *et al.* (1987) and duct cases AR2P5 and AR3P0 is less than 1.8%. However, the difference between the plane channel flow case and two test cases with lower AR values (duct cases AR1P0 and AR1P5) is 5.6%.

For a rectangular duct flow, the boundary layer developed over the narrow (vertical) wall is characteristically different from that developed over the wide (horizontal) wall. Furthermore, these two boundary layers interact with each other and induce secondary flow structures in a peripherally confined duct. In consequence, even the flow in the central symmetrical planes (at $y/\delta = 0.0$ or $z/\delta = 0.0$) of the duct can deviate from the 2-D ZPG boundary-layer flow, especially in the central horizontal plane (at $y/\delta = 0.0$), where the velocity scaling is based on the boundary layer developed over the narrow duct wall. As expected, as seen in the Fig. 3.10(c), although the profiles of streamwise RMS velocities in the ducts collapse well with each other in general. The peak value of the streamwise RMS velocity (of case AR2P5) is about 8.4% higher than that of a 2-D plane channel flow. Furthermore, as shown in the Fig. 3.10(d), it is apparent that the shear stress component $-\langle u'w'\rangle^+$ peaks about 16% higher than that in 2-D plane channel flow case of Kim *et al.* (1987). From Fig. Fig. 3.10(c), it is interesting to observe that the flow becomes increasing homogeneous for $z^+ > 200$, and profiles of the three turbulent intensities become flat and their magnitude become close to each other. Precisely, the magnitude of turbulent intensity is about 0.95 in the streamwise direction, and about 0.71 the other two directions.

3.4 Transport of Reynolds Stresses

To further refine the study of the AR effects on the Reynolds stresses, it is of interest to examine the budget balance of the Reynolds shear stress based on time- and streamwise-

averaging. The steady state Reynolds shear stress transport equation reads as:

$$\left(\underbrace{\langle u_k\rangle\frac{\partial\langle u_i'u_j'\rangle}{\partial x_k}}_{H_{ij}}\right)-\left(\underbrace{-\langle u_j'u_k'\rangle\frac{\partial\langle u_i\rangle}{\partial x_k}-\langle u_i'u_k'\rangle\frac{\partial\langle u_j\rangle}{\partial x_k}}_{P_{ij}}\right)-\left(\underbrace{\frac{2}{\rho}\langle p's_{ij}'\rangle}_{\Pi_{ij}}\right)+\left(\underbrace{2\nu\left\langle\frac{\partial u_i'}{\partial x_k}\frac{\partial u_j'}{\partial x_k}\right\rangle}_{\varepsilon_{ij}}\right)$$
$$-\left\{\underbrace{\frac{\partial}{\partial x_k}\left[-\langle u_i'u_j'u_k'\rangle-\frac{1}{\rho}\left(\langle p'u_j'\rangle\delta_{ik}+\langle p'u_i'\rangle\delta_{jk}\right)+\nu\frac{\partial\langle u_i'u_j'\rangle}{\partial x_k}\right]}_{D_{ij}}\right\}=0 \tag{3.3}$$

where the under-braced terms read in order as the convection H_{ij}, production P_{ij}, pressure strain Π_{ij}, viscous dissipation ε_{ij}, and total diffusion D_{ij}. Specifically, D_{ij} includes three sub-terms which are the turbulent, pressure, and viscous diffusion terms, respectively.

Figures 3.11 and 3.12 show the budget balance of the Reynolds shear stresses non-dimentionalized by u_τ^4/ν in the central vertical plane (at $z/\delta = 0.0$) and the central horizontal plane (at $y/\delta = 0.0$), respectively. In both Figs. 3.11 and 3.12, because of the highly-accurate numerical algorithm and fine grid resolutions used for the current DNS, the summation of the budget terms (H_{ij}^+, P_{ij}^+, Π_{ij}^+, ϵ_{ij}^+ and D_{ij}^+) on the left-hand-side of Eq. 3.3 recovers zero, the value of the right-hand-side of the Eq. 3.3. In order to make the presentation of the figure clear, the corresponding summation value (zero) of these budget terms is not shown in both Figs. 3.11 and 3.12. As seen in the Fig. 3.11(a), in the viscous sublayer (at $y^+< 5$), the positive contributions to the budge of streamwise Reynolds normal stress component $\langle u'u'\rangle$ mainly come from the total diffusion term D_{11}^+, whereas that from the production term P_{11}^+ is minor. Meanwhile, the negative contributions are from ε_{11}^+ and Π_{11}^+. In the buffer layer (at $5 <y^+< 30$), the streamwise production $\left(P_{11}^+\right)$ makes the dominant positive contributions to the budget balance of $\langle u'u'\rangle$, however, the contributions from the total diffusion term D_{11}^+ become negative. The magnitudes of P_{11}^+ and D_{11}^+ peak

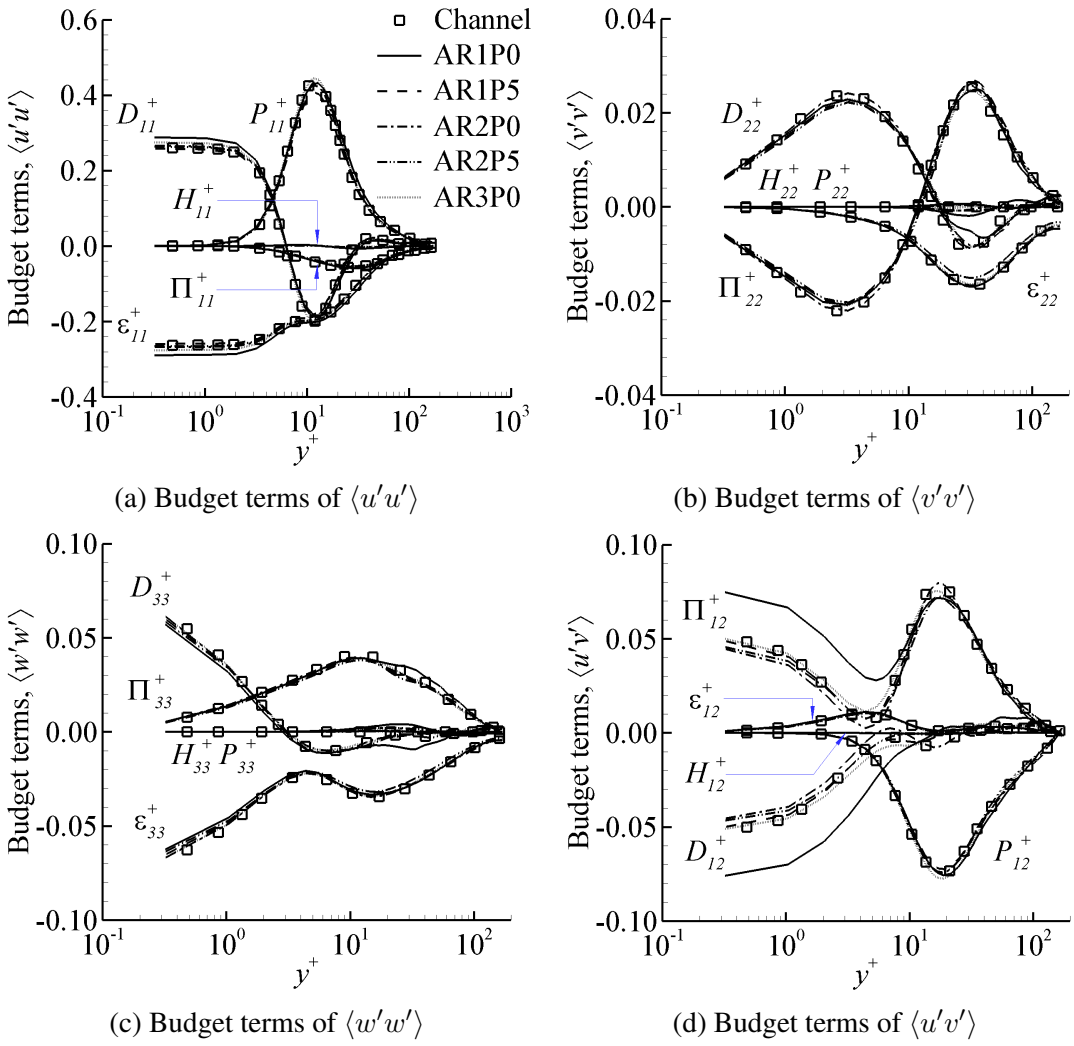

(a) Budget terms of $\langle u'u' \rangle$

(b) Budget terms of $\langle v'v' \rangle$

(c) Budget terms of $\langle w'w' \rangle$

(d) Budget terms of $\langle u'v' \rangle$

Figure 3.11: Budget balance of the Reynolds stresses non-dimentionalized by u_τ^4/ν in the central vertical plane at $z/\delta = 0.0$. For the purpose of comparison, the plane channel flow data of Kim *et al.* (1987) are also presented.

at $y^+ \approx 12$, where the maximum streamwise RMS velocity u_{rms}^+ occurs.

As is clear in the Figs.3.11(b)-(c), unlike the streamwise production $\left(P_{11}^+\right)$, the production terms in the other two directions (P_{22}^+ and P_{33}^+) barely make contributions into the normal stress budgets. Instead, the major contributors to the Reynolds normal stresses $\langle v'v' \rangle$ and $\langle w'w' \rangle$ are the pressure strain, viscous dissipation, and the total diffusion terms

(i.e., Π_{ii}^{+}, ε_{ii}^{+} and D_{ii}^{+}, respectively, for $i = 1$, 2 and 3, with no summation convention implied here). As shown in Fig. 3.11(b), the vertical pressure strain term Π_{22}^{+} first dominates the negative contributions to the vertical Reynolds normal stress budget balance of $\langle v'v' \rangle$ in the vicinity of the wall up to $y^{+} < 10$, but then contributes positively to the budget and peaks at $y^{+} \approx 30$. The trend of the total diffusion term D_{22}^{+} is the opposite to that of Π_{22}^{+}, as it first contributes positively and then negatively to the budget as the y^{+} value increases. The viscous dissipation term ε_{22}^{+} is the leading negative term in the region away from the wall for $y^{+} > 10$. Unlike Π_{22}^{+}, as shown in the Fig. 3.11(c), the spanwise pressure strain term Π_{33}^{+} consistently provides positive contributions to the budge balance of the Reynolds normal stress. Restricted by the continuity (Eq. (2.1)), $\Pi_{ii} \equiv 0$, and as such, the energy transferred between $\langle u'u' \rangle$, $\langle v'v' \rangle$ and $\langle w'w' \rangle$ through the pressure strain terms balances as $-\Pi_{11}^{+} = \Pi_{22}^{+} + \Pi_{33}^{+}$. This explains the trends of Π_{11}^{+}, Π_{22}^{+} and Π_{33}^{+} exhibited in Figs. 3.11(a)-(b).

From Fig. 3.11(c), it is clear that the viscous dissipation term ε_{33}^{+} is the largest in the near-wall region but becomes vanishingly small in the duct centre. Unlike the Reynolds normal stresses, the budget balance of the Reynolds shear stress $\langle u'v' \rangle$ shown in Fig. 3.11(d) exhibits considerably different features. As seen in the Fig. 3.11(d), the viscous dissipation term ε_{12}^{+} contributes positively to the shear stress budget in the viscous sublayer. Furthermore, the largest positive contribution comes from the pressure strain term Π_{12}^{+}. Meanwhile, the negative contributors are the total diffusion term D_{12}^{+} and production term P_{12}^{+}, which dominate regions inside and outside the viscous sublayer, respectively. In the region of away from the wall, the budget balance of $\langle u'v' \rangle$ is primarily balanced by the total diffusion term D_{12}^{+} and production term P_{12}^{+}. Particularly, the magnitudes of Π_{12}^{+} and P_{12}^{+} are are collocated at $y^{+} \approx 15$.

As is evident in Figs. 3.11(a)-(c), the profiles of different rectangular cases are, in general, insensitive to the AR value. However, as shown in Fig. 3.11(d), there is a relatively big discrepancy between the DNS result of a square duct (of AR $= 1.0$) and that of the plane

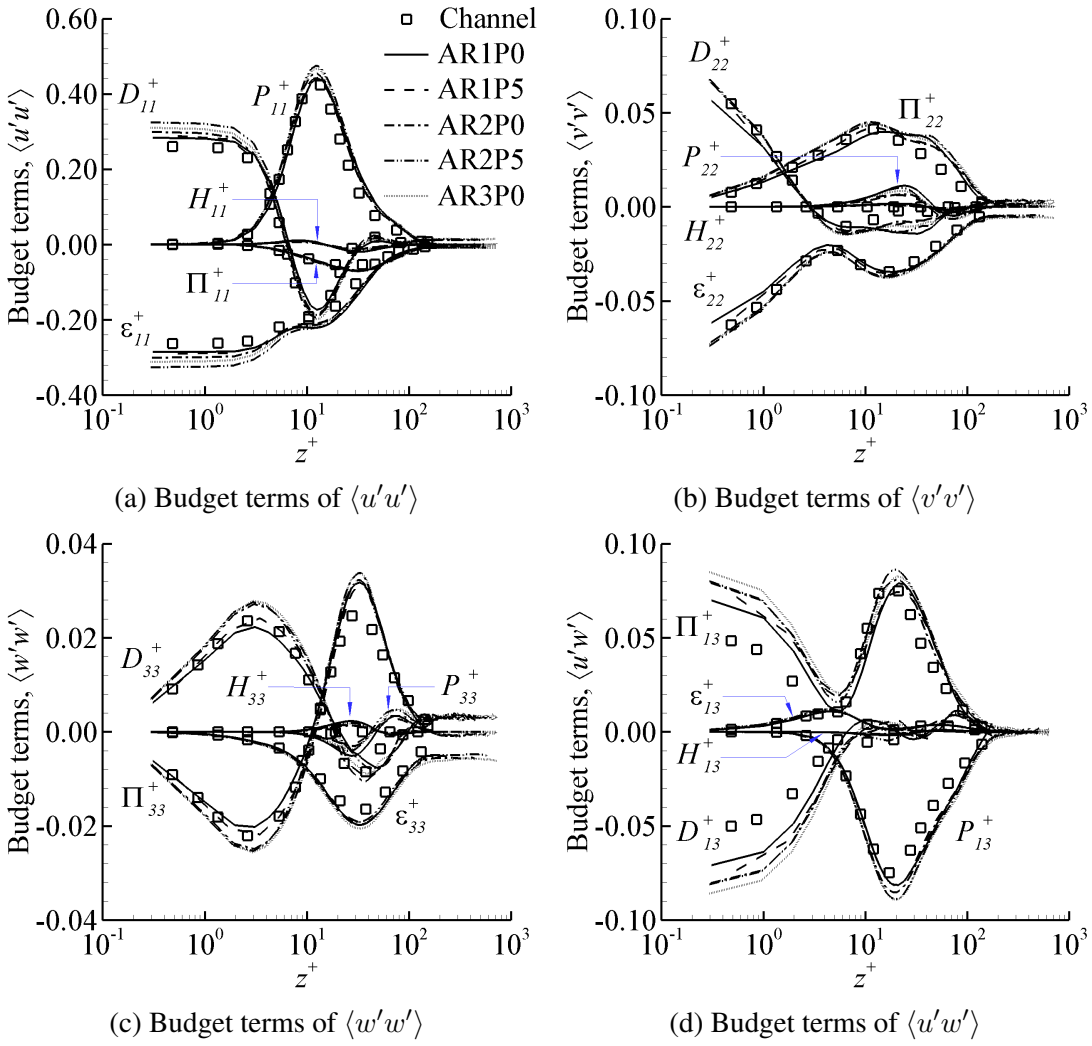

(a) Budget terms of $\langle u'u' \rangle$

(b) Budget terms of $\langle v'v' \rangle$

(c) Budget terms of $\langle w'w' \rangle$

(d) Budget terms of $\langle u'w' \rangle$

Figure 3.12: Budget balance of the Reynolds stresses non-dimentionalized by u_τ^4/ν in the central horizontal plane at $y/\delta = 0.0$. For the purpose of comparison, the plane channel flow data of Kim *et al.* (1987) are also presented.

channel flow of Kim *et al.* (1987). This indicates that the secondary flow pattern characteristic of a 3-D duct flow influences the turbulence statistics in the vertical symmetrical plane, such that they are different from those of a 2-D plane channel flow. However, it is apparent that the global agreement with the plane channel flow results improves with an increasing AR. In the central vertical plane (at $z/\delta = 0.0$) of the rectangular duct case of the highest aspect ratio (of AR $= 3.0$), the 2-D flow statistics are fully recovered, indicating that the

influence of the boundary layers developed over the two vertical sidewalls is minimal (in this central-symmetrical vertical plane). As seen in the Fig. 3.11(a), the streamwise normal stress budgets outside the viscous sublayer (at $y^+ > 5$) are independent of variations of the AR value. Furthermore, the maximum streamwise production budget, $(P_{11}^+)_{\max}$ is located at $y^+ \approx 12$, which agrees well with the known value of the plane channel and square duct flows (Kim *et al.*, 1987; Gavrilakis, 1992).

By comparing Fig. 3.12 with Fig. 3.11, it is clear that the profiles of Reynolds stress budgets w.r.t. z^+ are similar with those w.r.t. y^+. However, the magnitudes of the dominant budget terms are quite different. As seen in the Fig. 3.12(a), the streamwise production peak P_{11}^+ in duct cases increases slightly with an increasing AR. Precisely, the maximum P_{11}^+ in the case AR2P5 is 8.8% higher than that in the plane channel flow at $z^+ \approx 12$. Within the buffer layer of a side wall, it is apparent that the magnitudes of the total diffusion term D_{11}^+ and viscous dissipation term ε_{11}^+ of the duct cases increase as AR increases up to 2.5, and then decrease slightly in the case AR3P0. Furthermore, as shown in the Figs. 3.12(b)-(c), it is interesting to observe that the vertical and spanwise production terms (i.e., P_{22}^+ and P_{33}^+, respectively) contribute to the Reynolds normal stresses budge while they contribute nothing w.r.t. y^+. Consequently, it is concluded that the redistributed energy from $\langle u'u' \rangle$ (contributed by P_{22}^+ and P_{33}^+) is partially used to empower the turbulent flow structures near side wall.

From Fig. 3.12(c), it is clear that the budget balance of the spanwise Reynolds normal stress component is dominated by D_{33}^+ and Π_{33}^+ in the viscous sublayer, but by ε_{33}^+ and Π_{33}^+ in the buffer layers. The magnitudes of all these dominant terms deviate apparently from the those of the plane channel flow (Kim *et al.*, 1987), especially at their peak locations. Similar discrepancies between the dominant terms (Π_{13}^+, D_{13}^+ and P_{13}) and their counterpart plane-channel flow data can be observed in the budge balance of $\langle u'w' \rangle$ in Fig. 3.12(c). These discrepancies reflect the different mechanisms between a 2-D channel flow and a 3-D duct flow (in its central horizontal plane). Furthermore, as shown in Fig. 3.12(d), it

is clear that the magnitudes of Π_{13}^{+} and D_{13}^{+} both increase slightly with an increasing AR value. Other physical features shown in Fig. 3.12(d) for the budget balance of $\langle u'w' \rangle$ in the central horizontal plane of the duct are similar to those of $\langle u'v' \rangle$ in the central vertical plane of the duct exhibited in Fig. 3.11(c), and the discussions should be skipped in order to keep the thesis concise.

3.5 Turbulent structures

The turbulence coherent structures of a rectangular duct flow (of AR > 1.0) is qualitatively different from those of a square duct flow (Fang *et al.*, 2017) and a plane-channel flow (Kim *et al.*, 1987). This section focuses on analyzing the flow structures of case AR3P0, which has the largest AR value among the five test cases. Furthermore, current DNS employs the swirling strength criterion (λ_{ci}-criterion) of Zhou *et al.* (1999) for the visualization of flow structures. According to Zhou *et al.* (1999), the turbulent swirling strength, λ_{ci} is defined as the imaginary part of the complex eigenvalue of the velocity gradient tensor, and vortices visualized using the λ_{ci}-criterion are independent of the coordinate system.

Figure 3.13 illustrates the instantaneous iso-surfaces of turbulent swirling strength at $\lambda_{ci} = 1.2$. The zoomed-in figure panels (b) and (c) show the local hairpin structures contained in the indicated green boxes in panel (a). The blue color indicates positively-valued $\omega_x'^{+}$ and local counterclockwise (CCW) rotating motions, while the red color indicates negatively-valued $\omega_x'^{+}$ and local clockwise (CW) rotating motions. For a clear view of contours, only the bottom half of the duct is displayed. As shown in the zoomed-in figure panels (b) and (c), the captured vortexes are characterized as the hairpin structures that are described in Zhou *et al.* (1999) and Adrian (2007). This implies that the flow structures in the central regions of the duct (of AR $= 3.0$) are very similar to those observed in the turbulent plane channel flow. As shown in the Figs. 3.13(b) and (c), a large number of identified hairpin structures are in a complete “head-neck-legs" form as described by Robinson

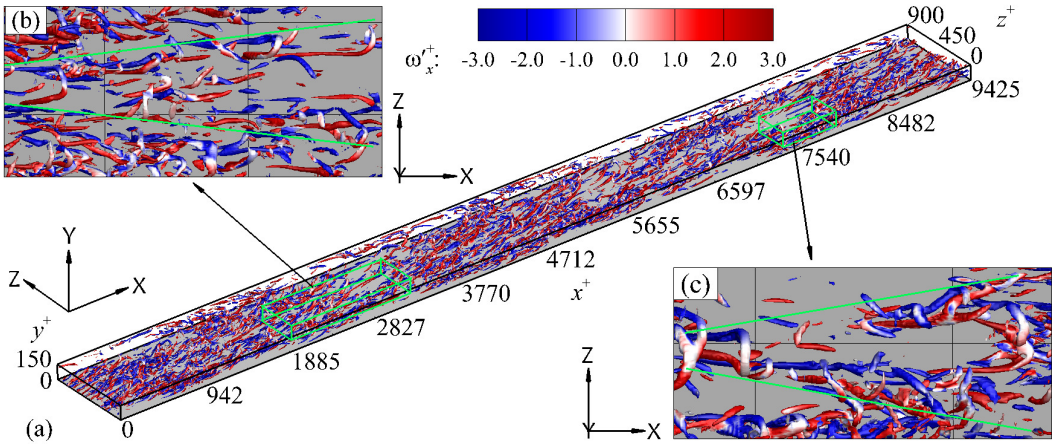

Figure 3.13: Instantaneous vortex structures captured using the λ_{ci} criterion and the local rotating strength of a vortex is visualized using the value of $\omega_x'^+$ in the case AR3P0. (a), 3-D iso-surface of turbulent swirling strength at $\lambda_{ci} = 1.2$; (b) and (c), top-view of local hairpin structures captured in two arbitrary indicated green boxes. The blue and red color represent the negative and positive values of the local instantaneous streamwise vorticity $\omega_x'^+$, respectively. Only the bottom half of the duct is displayed for a clear view of flow structures.

(1991). Furthrmore, as shown in Fig. 3.13(b), three or more hairpin structures are aligned in a row in the streamwise direction forming the so-called hairpin packets (Zhou *et al.*, 1999). In the region between two indicated green lines, it is also observed that the hairpin packets grow at the angle of 12°. Owing to the constraints from the two vertical sidewalls, hairpin packets are more populated in the central region of the bottom wall.

Figure 3.14 shows the partially enlarged hairpin structures extracted from Fig. 3.13(a) in the box of $L_x \times L_y \times L_z \in [1885,\ 2827] \times [0,\ 150] \times [300,\ 480]$. Fig. 3.14(b) demonstrates the contours of instantaneous shear stress, $-\left(u'v'\right)^+$ that was partially extracted in the x-y plane located at $z^+ \approx 400$. The vector field shown in this figure consists of the streamwise and vertical instantaneous velocity fluctuations u'^+ and v'^+, and they are displayed every 4 grid points in order to have a clear view of the vortical structures formed by the vectors. In Fig. 3.14(c), the instantaneous velocity streaks based on the instantaneous streamwise velocity u'^+ are shown in the horizontal (x-z) plane located at $y^+ \approx 30$. There

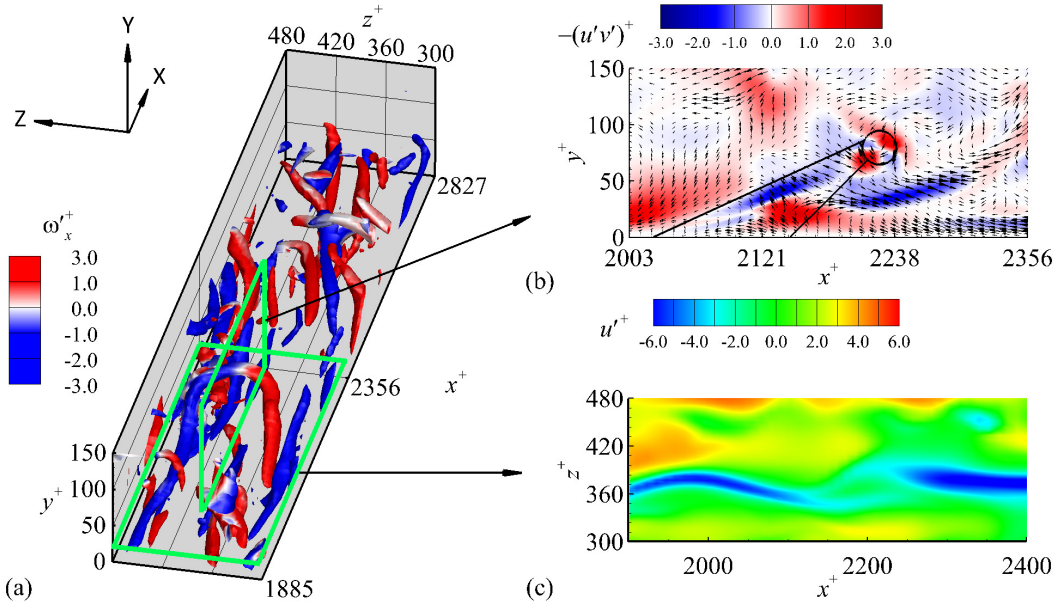

Figure 3.14: Enlarged hairpin structures partially extracted from Fig. 3.13(a). In (a), the 3-D instantaneous hairpin structures are extracted and displayed in the box of $L_x \times L_y \times L_z \in [1885,\ 2827] \times [0,\ 150] \times [300,\ 480]$. The hairpin structures are captured using the λ_{ci} criterion and the local rotating strength of a vortex is visualized using the value of $\omega_x'^+$. In (b), contours of instantaneous shear stress, $-(u'v')^+$ displayed in x-y plane at $z^+ \approx 400$, superimposed with the turbulent velocity vector field. The vector field is shown using the streamwise and vertical instantaneous velocity fluctuations u'^+ and v'^+, displaying at every 4 grid points in order to have a clear view. In (c), the instantaneous near-wall streaks based on the contours of the streamwise velocity u'^+ displayed in x-z plane at $y^+ \approx 30$, superimposed with hairpin structures off the displaying plane.

are two inclined lines shown in Fig. 3.14(b), the top inclined-line shows a strong shear layer created by the Reynolds shear stress. Specifically, it is apparent that the positive and negative shear stresses are separated by the line. The lower inclined-line with the circle indicates that the head of the captured hairpin structure is oriented at $45°$ with respect to the streamwise direction, which is consistent with the observation of Head & Bandyopadhyay (1981) and Adrian *et al.* (2000). As shown in the Fig. 3.14(c), the low-speed streak under the captured hairpin was found to be broken. This is because the mechanism of turbulent burst as described in Robinson (1991). As such, the central vertical section of the hairpin would be separated by the events of ejections (Q2-event) and sweeps (Q4-event).

The Q2-event combined with vertical velocity (v') pops up the hairpin structure, breaking up the low-speed streak underneath; whereafter, re-forming a new low-speed streak due to the Q4-event.

In fact, the turbulent burst mechanism is not randomly exhibited in case AR3P0, rather, it is the consequence of the existence of spanwise homogeneity. In the previous discussion of the spanwise profiles of the turbulent intensities and the Reynolds stress budgets, a short spanwise homogeneity in the center was observed in the rectangular duct of AR $= 3.0$. Particularly, analogous to the mechanism in a 2-D plane channel flow, the spanwise homogeneity in the central region of the rectangular duct is responsible for the appearance of the hairpin structures. In order to refine the study, it is useful to further examine the streamwise pre-multiplied 1-D energy spectrum, ϕ_{uu}, defined as $\phi_{uu} = k_x E_{uu}$, where E_{uu} is 1-D energy spectrum (defined as product of the Fourier transfer of the streamwise velocity and its conjugate, $\langle \hat{u}\hat{u}^* \rangle$), and k_x is the streamwise wavenubmer.

Figures 3.15 and 3.16 show the isopleths of the streamwise pre-multiplied 1D energy spectrum w.r.t. the streamwise wavelength, λ_x^+, for ducts of AR $= 1.0$ and 3.0 at four different vertical positions varying from $y^+ \approx 5$ to 150, corresponding to the viscous sublayer, buffer layer, logarithmic layer, and central plane of the domain. Symbols "$\times$" demarcates the peak position of ϕ_{uu}^+. Three isopleth levels are displayed, corresponding to 62.5%, 25.0% and 12.5% of its peak value of ϕ_{uu}^+. Among these three isopleths, eddy motions of wavelengths enclosed by that corresponding to 62.5% of the peak value of ϕ_{uu}^+ represent the most energetic vortex cores, which clearly, have all been well captured in Figs. 3.15 and 3.16. In contrast, eddy motions enclosed by the isopleth corresponding to 12.5% of the peak value of ϕ_{uu}^+ are of a relatively low TKE level and cover a very wide range of wavelengths. Although the duct length ($L_x = 20\pi\delta$) used in this DNS study is the longest of the current literature, it is not sufficient to fully capture elongated eddy motions at this low TKE level in regions near the top and bottom walls, as clearly shown in Figs. 3.15(a)-(b) and 3.16(a)-(b). This issue of proper computational domain size has been thoroughly

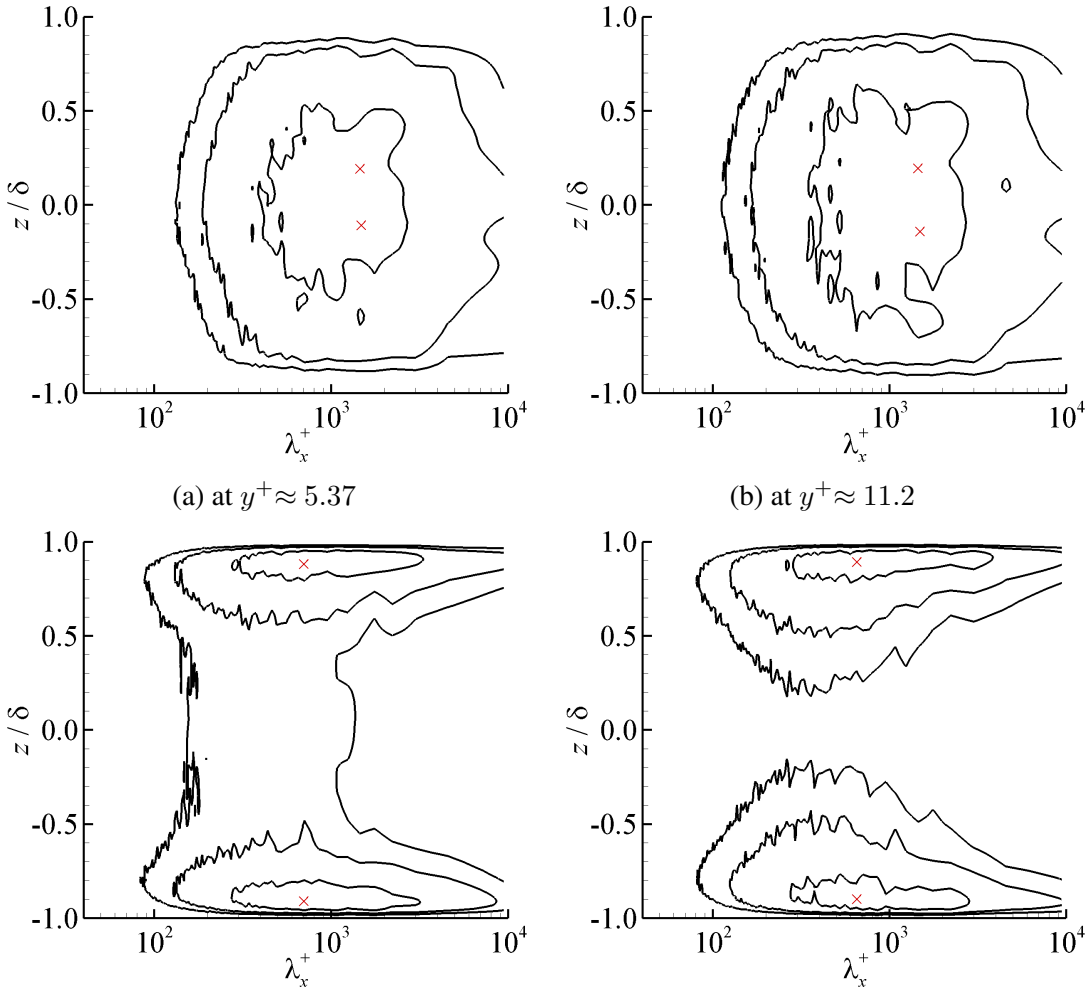

(a) at $y^+ \approx 5.37$ (b) at $y^+ \approx 11.2$

(c) at $y^+ \approx 99.9$ (d) at $y^+ = 150$

Figure 3.15: Isopleths of the streamwise pre-multiplied 1-D energy spectrum ϕ_{uu}^+ w.r.t. the streamwise wavelength (λ_x^+) in horizontal planes of the square duct (of AR$= 1.0$) at four different vertical positions varying from $y^+ \approx 5$ to 150, corresponding to the viscous sub-layer, buffer layer, logarithmic layer, and central horizontal plane of the domain. Symbol "$\times$" indicates the maximum value of ϕ_{uu}^+. Three contour levels of energy spectrum are plotted, which correspond to 62.5%, 25.0% and 12.5% of its peak value.

discussed in section §3.1. From Figs. 3.15 and 3.16, it is clear that the shortest eddies (eddy motions of the shortest wavelengths) corresponding to the isopleth of 12.5% of the peak of ϕ_{uu}^+ have been well captured. Interestingly, as shown in Figs. 3.15(c)-(d) and 3.16(c)-(d), the streamwise length scales of the largest eddies corresponding to this low TKE level re-

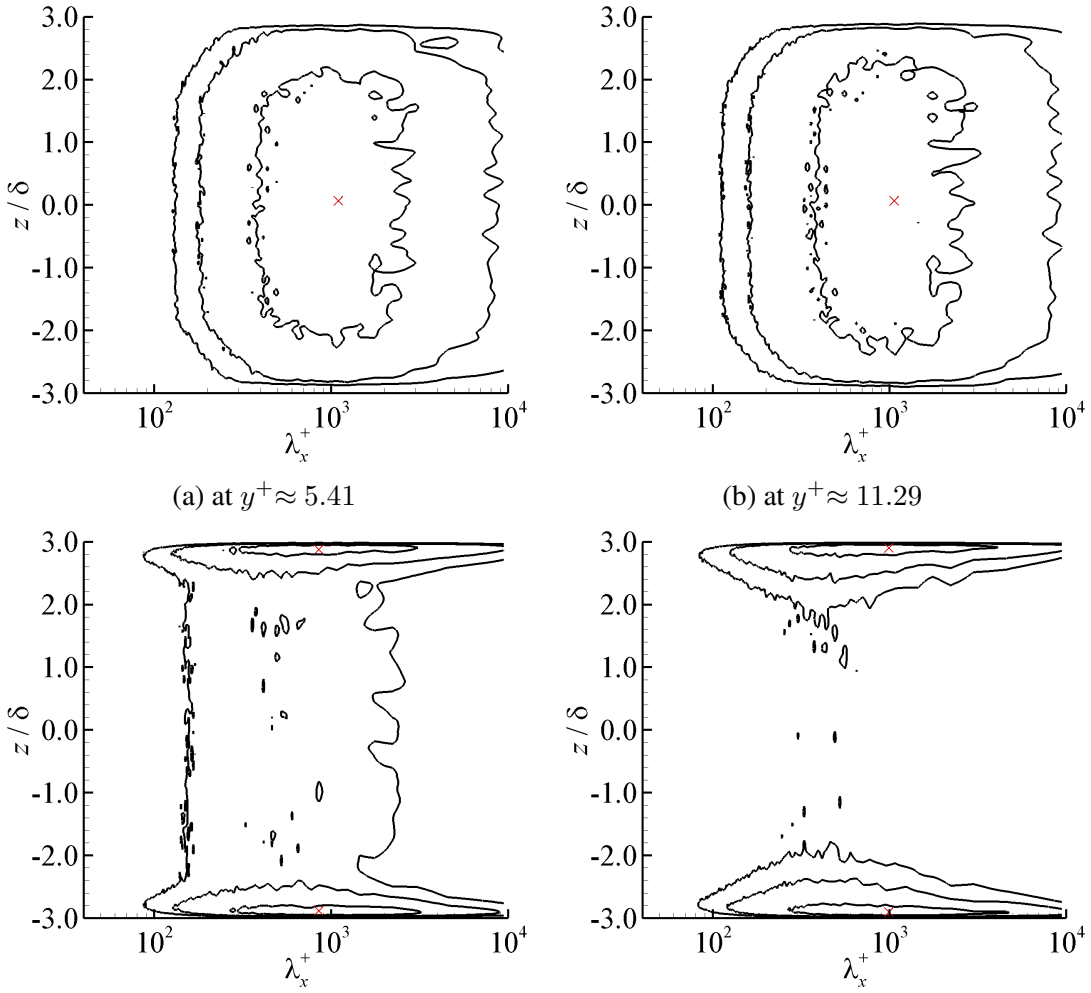

(a) at $y^+ \approx 5.41$ (b) at $y^+ \approx 11.29$

(c) at $y^+ \approx 100.97$ (d) at $y^+ = 150$

Figure 3.16: Isopleths of the streamwise pre-multiplied 1-D energy spectrum ϕ^+_{uu} w.r.t. the streamwise wavelength (λ^+_x) in horizontal planes of the duct (of AR$= 3.0$) at four different vertical positions varying from $y^+ \approx 5$ to 150, corresponding to the viscous sublayer, buffer layer, logarithmic layer, and central horizontal plane of the domain. Symbol "$\times$" indicates the maximum value of ϕ^+_{uu}. Three contour levels of energy spectrum are plotted, which correspond to 62.5%, 25.0% and 12.5% of its peak value.

duce significantly with an increasing y^+ value, such that they are well captured by DNS in the duct center.

As seen in Fig. 3.15, spanwise homogeneity (i.e., being invariant with z/δ) can be

barely observed in the isopleth pattern of ϕ^+_{uu}. In contrast, as shown in Figs. 3.16(a)-(c), spanwise homogeneity is clearly maintained in the near-wall region for $y^+ \leq 100.97$. This indicates that owing to the comparatively large AR value of 3.0, the characteristics of the boundary layer in the central region of the rectangular duct (of case AR3P0) is expected to be analogous to those of 2-D plane channel, such that the hairpin structures may grow and evolve along the top and bottom walls. The width of the spanwise homogeneity region is around 270 wall unites.

By comparing Fig. 3.15(a) with Fig. 3.16(a), and Fig. 3.15(b) with Fig. 3.16(b), it is clear that the AR value has a significant effect on the mode of ϕ^+_{uu}. In a square duct (of AR $= 1.0$), as shown in Figs. 3.15(a) and 3.15(b), a dual-peak pattern is observed, which is a result of perfect geometrical symmetry of the boundary layers developed over four equal-width sidewalls. However, as shown in in Figs. 3.16(a) and 3.16(b), there is only one single peak at $z/\delta = 0.0$ in the near-wall region (at $y^+ = 5.41$ and 11.29). This peak of ϕ^+_{uu} corresponds to elongated near-wall streaky structures analyzed previously in Figs. 3.13 and 3.14. This indicates that in the region near the top and bottom walls (more specifically, in the viscous sublayer and buffer layer), the boundary layers are dominated by the two wide horizontal duct walls, and the influence from the two narrow vertical sidewalls is minimal. This, again, is a reflection of the quasi 2-D spanwise homogeneity in the central region of boundary layers developed over the top and bottom walls of the rectangular duct of AR $= 3.0$.

Away from the top and bottom walls, as shown in Figs. 3.15(c)-(d) and Figs. 3.16(c)-(d), the isopleths of the streamwise energy spectrum ϕ^+_{uu} exhibits two symmetrical peaks close to the two vertical sidewalls (at $z/\delta = \pm 3.0$). This indicates that in the horizontal plane far off the wall, the most energetic eddy motions are close to the two vertical sidewalls, corresponding to the streaky structures developed over these sidewalls. From Figs. 3.15(a)-(b), it is evident that for the square duct case, the characteristic length scale of the most energetic eddies (corresponding to the mode of the ϕ^+_{uu} distribution) is around $\lambda^+_x = 1400$

in the region near the top and bottom walls. However, Fig. 3.15(d) shows that as the value of y^+ increases, the characteristic length scale decreases to around $\lambda_x^+ = 650$ in the central horizontal plane of the duct. This is because of the boundary layer of the side walls that interact with the boundary layers of top and bottom walls. In contrast, as seen in Fig. 3.16, the characteristic length scale of the most energetic eddies is less sensitive to the wall distance (i.e., the y^+ value) and is always around $\lambda_x^+ = 1000$, indicating that the sidewall influences are dramatically reduced. Figs. 3.15 and 3.16 clearly show the AR effect on the length scales of dominant eddy motions confined within a rectangular duct.

Chapter 4

Conclusions and future studies

This chapter summarizes the major conclusions on the current DNS study of turbulent flows in the rectangular ducts of different aspect ratio values, in terms of the research tools and results. The high-accuracy spectral elements code, “Semtex", is employed for conducting DNS in this thesis. The algorithm is given in Appendix A, and a recommendation on implementing the Semtex code will also be provided in this chapter.

4.1 Conclusions on DNS of turbulent flow in a rectangular duct of varying AR

DNS has been performed to investigate the fully-developed turbulent flows confined within rectangular ducts of different AR values (ranging from 1.0 to 3.0) at a fixed Reynolds number $Re_\tau = 150$.

Turbulent flows confined within the rectangular ducts (of AR $= 3.0$) of different streamwise computational domain sizes, $L_x = 2\pi\delta$, $4\pi\delta$, $8\pi\delta$, and $20\pi\delta$, are simulated to examine the impact of the streamwise domain size on the predictive accuracy of turbulence statis-

tics. It is observed that the turbulence statistics are sensitive to the streamwise computational domain sizes, a conclusion that is consisted with the findings of Gavrilakis (1992). Through a direct comparison of two-point autocorrelations (R_{uu} and R_{vv}) and streamwise pre-multiplied 1-D energy spectrum (ϕ^+_{uu}), the obtained results of the rectangular duct computed in the computational domain size of $L_x = 20\pi\delta$ are deemed as the most reliable. Specifically, within such a long domain size, most energetic eddy motions (up to 25% of the maximum ϕ^+_{uu}) are contained in the domain.

In a rectangular duct flow, there are four boundary layers developing over the four side walls, dynamically interacting with each other. As result, the secondary flows of Prandtl's second kind appear as one pair of counter-rotating vortices in each corner of the rectangular duct. Particularly, it is observed that the streamwise mean secondary flow vortices are symmetrical about the diagonal line in the square duct case. As the AR value increases, the streamwise vortices near the top and bottom walls extend towards to the vertical duct centre. Following Vinuesa *et al.* (2014), the vortex cores are detected using the local minima of cross-stream velocity ($\langle u_{\text{cs}} \rangle^+$). By tracking down the movement of the vortex core near the bottom wall, it is discovered that the distance from the vortex core to the sidewall and to the bottom wall follows a linear relationship as $y^+ = 0.4z^+ + 0.23$ for AR $\in [1.0, 3.0]$. Furthermore, in the comparison with turbulent square duct flow results of Pinelli *et al.* (2010) at $Re_\tau \geq 100$, it is found that this linear relationship holds as the vortex core moves around. Therefore, it is concluded that the movement of the vortex core near bottom wall is independent from the larger Reynolds numbers ($Re_\tau \geq 100$).

It is apparent that the mean streamwise velocity profile in the central horizontal plane of the rectangular ducts becomes increasingly similar to that characteristic of a 2-D ZPG boundary layer as AR increases. Furthermore, as AR becomes greater than 2.0, the discrepancy in the magnitude of RMS velocities between the test cases and the plane channel flow of Kim *et al.* (1987) reduces significantly. In particular, it is found that the difference in the turbulent intensities and Reynolds shear stress w.r.t. y^+ between case AR3P0 and the

plane channel flow of Kim *et al.* (1987) is minimum.

In the rectangular duct of AR $= 3.0$, the hairpin structures are visualized in the central regions of the duct using the λ_{ci}-criterion. The captured hairpin structures are characterized in a complete form of a “leg-neck-head" similar to those exhibited in a plane channel flow. In fact, the appearance of hairpins is the consequence of the existence of spanwise quasi-homogeneity. By using the streamwise pre-multiplied 1-D energy spectrum, this spanwise homogeneity is demonstrated. Specifically, the width of spanwise homogeneous region is about $\Delta z^+ = 270$. Moreover, it is highlighted that the characteristic length scale of the most energetic eddies is maintained at $\lambda_x^+ \approx 1,000$ w.r.t. y^+, which indicates that the influences of sidewalls dramatically reduces with an increasing AR value.

4.2 Future studies

In the future studies, two new research directions can be considered, which represent natural extensions of this thesis:

- Rectangular duct flows under system rotations. A system rotation imposed on the rectangular duct flow necessarily induces Coriolis forces. As body forces, the appearance of the Coriolis forces drastically alter the turbulent flow field and structures. The challenges involved in this new research direction include significantly enhanced computational efforts and deeper understanding of the physical mechanisms of the rotating turbulence field and its dynamic interactions with the four boundary layers developed over the four duct walls.
- Rectangular duct flows with heat transfer. In this new research direction, heat transfer will be considered. Given the structure of the spectral-element code, to begin, it would be more suitable to treat the thermal energy as a passive scalar, i.e., by ignoring the buoyancy effect. The analysis will enrich the understanding of both momentum and heat transfer in the rectangular ducts of different AR values.

To achieve the above new goals, the major computing part of the Semtex code needs to be further developed on the implementations of the external forces. Moreover, the post-processing code needs also to be implemented for turbulence statistics influenced by the system rotation/heat transfer. In addition, the current code stores the whole instantaneous 3-D flow fields, which requires enormous data storage space for each simulation (about 3 to 4 TB data per case). Therefore, in the future, the storage method needs to be reconsidered. It would be more efficient to compute directly the statistical moments of the flow and scalar fields, and store only the obtained statistics on a server.

Appendix: A
Spectral-Element Method

The current DNS study is conducted using the “Semtex" code publicly shared by Blackburn & Shewin (2004). The code is written primarily with programming languages C++ and FORTRAN. To well understand the main computing cores such as matrix multiplication, I have studied every single subroutine in the code. Also, in order to produce the turbulence statistics, I have used C++ to develop the post-processing scripts for processing the obtained data using an object-oriented programming approach. For instance, the main code will produce the instantaneous files that contain the instantaneous velocity and pressure fields. The post-processing code then needs to read the instantaneous fields to produce turbulence statistics including the mean flows, TKE, RMS velocities, Reynolds stresses and its transport equations, two-point autocorrelations, pre-multiply energy spectra, and the λ_{ci} values for visualizing flow structures, etc. This appendix provides a detail description of the temporal and spatial discretizations implemented in the Semtex code.

A.1 Time-splitting algorithm

The governing equations include the continuity and the Naiver-Stokes equations, which in the context of an incompressible flow can be written as

$$\begin{aligned} &\nabla \cdot \mathbf{u} = 0, \\ &\frac{\partial \mathbf{u}}{\partial t} + \mathbf{N}(\mathbf{u}) = -\frac{1}{\rho}\nabla p + \nu \nabla^2 \mathbf{u} + \mathbf{f}, \end{aligned} \tag{A. 1}$$

where the nonlinear convective term, $\mathbf{N}(\mathbf{u})$ can be represented as follows as:

$$\mathbf{N}(\mathbf{u}) = \mathbf{u} \cdot \nabla \mathbf{u}, \tag{A. 2}$$

$$\mathbf{N}(\mathbf{u}) = \nabla \cdot (\mathbf{u}\mathbf{u}), \tag{A. 3}$$

$$\mathbf{N}(\mathbf{u}) = \frac{1}{2}\left[\mathbf{u} \cdot \nabla \mathbf{u} + \nabla \cdot (\mathbf{u}\mathbf{u})\right], \tag{A. 4}$$

$$\mathbf{N}(\mathbf{u}) = (\nabla \times \mathbf{u}) \times \mathbf{u} + \frac{1}{2}\nabla(\mathbf{u} \cdot \mathbf{u}), \tag{A. 5}$$

which are called in order as the convective, divergence, skew-symmetric and rotational forms. The different forms of $\mathbf{N}(\mathbf{u})$ are identical in the continuous mathematics, but possess significantly different properties after discretization. As the de-aliasing technique is employed, the results with all four forms are almost identical; however, the de-aliasing can be expensive to implement and it is usually deactivated for the coarse mesh grid. In particular, although the use of the skew-symmetric form (Eq. (A. 4)) in computations is expensive, it is tolerable for the aliasing errors. Considering the stability and computational costs, the current thesis employed the convective and divergence forms by considering the computing resources (Zang, 1991).

The temporal discretization uses “stiffly stable" integration as follows,

$$\frac{\partial u^{(n+1)}}{\partial t} = \frac{1}{\Delta t}\sum_{q=0}^{k} \alpha_q u^{(n+1-q)}, \tag{A. 6}$$

where α_q is the chosen weight at k. Normally, when $k = 1$, Eq. (A. 6) reads as the backward Euler equation. The region of stability shrinks with an increase of value k. In particular, when $k = 2$, known as A-stable, Eq. (A. 6) well balances the CFL stability and spatiotemporal accuracy. When we decouple the velocity and pressure, the sub-steps are described as follows:

$$\frac{\mathbf{u}^* - \mathbf{u}^n}{\Delta t} = \sum_{q=0}^{k-1} \beta_q \left[\mathbf{N}\left(\mathbf{u}^{(n-q)}\right) + \mathbf{f}^{(n-q)}\right], \tag{A. 7}$$

$$\frac{1}{\rho}\nabla^2 p^{(n+1)} = \frac{\nabla \cdot \mathbf{u}^*}{\Delta t}, \tag{A. 8}$$

$$\frac{\mathbf{u}^{**} - \mathbf{u}^*}{\Delta t} = -\frac{1}{\rho}\nabla \cdot p^{(n+1)}, \tag{A. 9}$$

$$\frac{\mathbf{u}^{(n+1)} - \mathbf{u}^{**}}{\Delta t} = \nu\nabla^2 \mathbf{u}^{(n+1)}, \tag{A. 10}$$

where β_q is the chosen weight at k, and $\mathbf{u}^*$ and $\mathbf{u}^{**}$ are intermediate velocity fields. Note that the boundary condition applied in Eq. (A. 8) is defined as follow

$$\frac{1}{\rho}\frac{\partial p^{(n+1)}}{\partial n} = -\mathbf{n} \cdot \sum_{q=0}^{k-1} \beta_q \left[\mathbf{N}\left(\mathbf{u}^{(n-q)}\right) + \nu\nabla \times \nabla \times \mathbf{u}^{(n-q)}\right]. \tag{A. 11}$$

The boundary condition in Eq. (A. 10) is imposed.

A.2 Spatial discretization

A.2.1 Method of weighted residual (MWR)

In Semtex, quantities in the periodic/homogenous direction, assuming z-direction, are transformed into the Fourier space. Meanwhile, quantities in the cross-stream plane are interpolated using the quadrilateral spectral-element method based on GLL Lagrange interpolates in x- and y-directions. As such, Eqs. (A. 8) and (A. 10) can be rewritten as

$$\frac{1}{\rho}\left[\nabla^2_{xy}\hat{p}^{(n+1)} - k_z^2\hat{p}^{(n+1)}\right] = \nabla\cdot\left(\frac{\hat{\mathbf{u}}^*}{\Delta t}\right), \tag{A. 12}$$

$$\nabla^2_{xy}\hat{\mathbf{u}}^{(n+1)} - \left(\frac{1}{\nu\Delta t} + k_z^2\right)\hat{\mathbf{u}}^{(n+1)} = -\frac{\hat{\mathbf{u}}^{**}}{\nu\Delta t}, \tag{A. 13}$$

where the Laplace operator in x and y-directions is defined as $\nabla^2_{xy} = \partial^2_{x^2} + \partial^2_{y^2}$, and k_z represents the wavenumber in z-direction. Note that the quantities in form of $\hat{(\cdot)}$ are expressed in the Fourier space. To generalize the above equation, 2-D Helmholtz equation in a general form can be employed and expressed as

$$\nabla^2 u - \lambda u = f, \tag{A. 14}$$

where λ is a real number and f is a general constant. In a domain of Ω, we take the integration of Eq. (A. 14) with a multiplication of the weight function w. Using the integration by parts (IBP) on the ∇^2, we can express the integration of Eq. (A. 14) as

$$\int_\Omega (\nabla u\cdot\nabla w + \lambda uw)\, d\Omega = -\int_\Omega fw\, d\Omega + \oint_{\partial\Omega} hw\, d(\partial\Omega), \tag{A. 15}$$

where h is defined as $n \cdot \nabla u$, satisfying the Neumann boundary condition. To discretize globally, we start with the basis function $\mathcal{N}(x)$

$$u(x) = \sum_{j=1}^{N} u_j \mathcal{N}_j(x), \tag{A. 16}$$

$$w(x) = \sum_{i=1}^{N} w_i \mathcal{N}_i(x), \tag{A. 17}$$

where N is total number of elements. To satisfy the Dirichlet boundary condition, the weight function must be zero because of the unknown velocity gradient. Assuming $w_i = 1$, we could rearrange above equations with Eq. (A. 15) as one equation for each global weight function, i.e.

$$\begin{aligned} &\sum_{j=1}^{N} \int_{\Omega} u_j \left[\nabla \mathcal{N}_j(x) \cdot \nabla \mathcal{N}_i(x) + \lambda \mathcal{N}_j(x) \mathcal{N}_i(x)\right] d\Omega \\ &= -\int_{\Omega} f_j \mathcal{N}_j(x) \mathcal{N}_i(x)\, d\Omega + \oint_{\partial\Omega} h_j \mathcal{N}_j(x) \mathcal{N}_i(x)\, d(\partial\Omega), \\ &= \sum_{j=1}^{N} H_{ij} u_j. \qquad \longleftarrow \text{“Helmhotlz”} \end{aligned} \tag{A. 18}$$

Now, we consider to partition the whole domain of Ω into sub-domain of Ω_e for each element, using **Integral(Sum) = Sum(Integrals)** as $\int_{\Omega} (\cdot)\, d\Omega = \sum_{e=1}^{N_e} \int_{\Omega_e} (\cdot)\, d\Omega_e$. Consequently, Eq. (A. 18) can be rearranged elementally as

$$\begin{aligned} &\int_{\Omega_e} \left[\nabla \mathcal{N}_j(x) \cdot \nabla \mathcal{N}_i(x) + \lambda \mathcal{N}_j(x) \mathcal{N}_i(x)\right] d\Omega_e = H^e_{ij} \\ &= -\int_{\Omega_e} f_j \mathcal{N}_j(x) \mathcal{N}_i(x)\, d\Omega_e + \oint_{\partial\Omega_e} h_j \mathcal{N}_j(x) \mathcal{N}_i(x)\, d(\partial\Omega_e). \end{aligned} \tag{A. 19}$$

Hence, in a 2-D form, the left-hand side of above equation can be expressed as

$$\begin{aligned} H^e_{ab} &= \int_{\Omega_e} \left[\nabla \mathcal{N}_b(x) \cdot \nabla \mathcal{N}_a(x) + \lambda\, \mathcal{N}_b(x) \mathcal{N}_a(x)\right]\, d\Omega_e \\ &= \int_y \int_x \left[\nabla \mathcal{N}_{b_{xy}} \cdot \nabla \mathcal{N}_{a_{xy}} + \lambda\, \mathcal{N}_{b_{xy}} \mathcal{N}_{a_{xy}}\right]\, dx_e dy_e. \end{aligned} \tag{A. 20}$$

A.2.2 Discretization in a 2-D quadrilateral element

In order to discrete integrations in Eq. (A. 20), the discretization in a quadrilateral element needs to be introduced base on the understanding of MWR procedure.

1. **Construction of one set of nodal basis functions:**

   In the range $[-1, 1]$, we choose nodal basis functions as Lagrange polynomials as $\{\Psi_i(\xi)\}$. The polynomials satisfy $\Psi_i(\xi_j) = \delta_{ij}$ for $\{i, \xi_j, j = 0, 1, \cdots, N\}$, which are the GLL quadrature points, corresponding to the zeros of $(1 - \xi^2)L'_N(\xi)$ with $L'_N(\xi)$ being the Legendre polynomial of order N.

2. **Construction of one set of trial functions to satisfy the boundary conditions:**

   The general trial functions can be set as

   $$u(\xi_1, \xi_2) = \sum_{i=0}^{N} \sum_{j=0}^{N} u_{ij} \Psi_i(\xi_1) \Psi_j(\xi_2), \tag{A. 21}$$

   where $\Psi_i(\xi_1)$ and $\Psi_j(\xi_2)$ represent the basis functions, and u_{ij} denotes the coefficients.

3. **Construction of one set of weight functions:**

   Employing the Galerkin MWR, in the standard canonical domain $[-1, 1] \times [-1, 1]$, the weight function yields the following equation which is the same as the basis

functions

$$w_{mn} = \int_{-1}^{1}\int_{-1}^{1} \Psi_m(\xi_1)\Psi_n(\xi_2)d\xi_1 d\xi_2. \tag{A. 22}$$

Subscripts m and n are the GLL quadrature points, satisfying $m, n = 0, 1, \cdots, N$.

4. **Construction of functions algebraically:**

In order to perform quadratures in a general system instead of (x, y) in Cartesian system, we apply the Jacobian of mapping in each element as

$$J = \begin{bmatrix} \dfrac{\partial x}{\partial \xi_1} & \dfrac{\partial x}{\partial \xi_2} \\ \dfrac{\partial y}{\partial \xi_2} & \dfrac{\partial y}{\partial \xi_1} \end{bmatrix}. \tag{A. 23}$$

Then, in the standard canonical domain $[-1, 1] \times [-1, 1]$, the trial function can be expressed as

$$\begin{aligned}
\int_\Omega u(x, y)dxdy &= \int_\Omega u(\xi_1, \xi_2)Jd\xi_1 d\xi_2 \\
&= \sum_{i=0}^{N}\sum_{j=0}^{N} u_{ij}\int_{-1}^{1}\int_{-1}^{1} J(\xi_1, \xi_2)\Psi_i(\xi_1)\Psi_j(\xi_2)d\xi_1 d\xi_2 \\
&= \sum_{i=0}^{N}\sum_{j=0}^{N} u_{ij}\sum_{p=0}^{N} w_p \sum_{q=0}^{N} w_q J(\xi_{1p}, \xi_{2q})\Psi_i(\xi_{1p})\Psi_j(\xi_{2q}) \\
&= \sum_{i=0}^{N}\sum_{j=0}^{N} u_{ij}\sum_{p=0}^{N} w_p \sum_{q=0}^{N} w_q J(\xi_{1p}, \xi_{2q})\delta_{ip}\delta_{jq} \\
&= \sum_{i=0}^{N}\sum_{j=0}^{N} u_{ij} w_i w_j J_{ij} \\
&= \mathbf{w}^T\mathbf{u},
\end{aligned} \tag{A. 24}$$

where

$$\mathbf{w}^T = [w_0 w_0 J_{00}, w_1 w_0 J_{10}, \cdots, w_N w_N J_{NN}]^T$$
$$\mathbf{u} \quad = [u_{00}, u_{10}, \cdots, u_{N0}, u_{01}, u_{11}, \cdots, u_{NN}]^T$$

Note that the Gaussian quadrature rule and property of $\Psi_i(\xi_j) = \delta_{ij}$ are applied for the above equation. The derivative of $u(\xi_1, \xi_2)$ can be expressed as

$$\frac{\partial u(\xi_1, \xi_2)}{\partial \xi_1} = \sum_{i=0}^{N} \sum_{j=0}^{N} u_{ij} \frac{\partial \Psi_i(\xi_1)}{\partial \xi_1} \Psi_j(\xi_2) = \hat{\mathbf{D}} \otimes \hat{\mathbf{I}} \mathbf{u} = \mathbf{D}_1 \mathbf{u}, \tag{A. 25}$$

$$\frac{\partial u(\xi_1, \xi_2)}{\partial \xi_2} = \sum_{i=0}^{N} \sum_{j=0}^{N} u_{ij} \Psi_i(\xi_1) \frac{\partial \Psi_j(\xi_2)}{\partial \xi_2} = \hat{\mathbf{I}} \otimes \hat{\mathbf{D}} \mathbf{u} = \mathbf{D}_2 \mathbf{u}, \tag{A. 26}$$

where the $\hat{\mathbf{D}}_k = \dfrac{\partial \Psi_i(\xi_k)}{\partial \xi_k}$ denotes the differentiation matrix, and the symbol $\otimes$ is the Kronecker product operator. With respect to x and y, the differentiation matrix can be written as

$$\mathbf{D}_x = \Lambda \left(\frac{\partial \xi_1}{\partial x} \right) \mathbf{D}_1 + \Lambda \left(\frac{\partial \xi_2}{\partial x} \right) \mathbf{D}_2, \tag{A. 27}$$

$$\mathbf{D}_y = \Lambda \left(\frac{\partial \xi_1}{\partial y} \right) \mathbf{D}_1 + \Lambda \left(\frac{\partial \xi_2}{\partial y} \right) \mathbf{D}_2, \tag{A. 28}$$

where function $\Lambda(f_{ij})$ returns a matrix of rank $(N+1)^2$ with the diagonal compo-

nents being vector f_{ij}. Now, the general trial function can be expressed as

$$\begin{aligned}(u(\xi_1,\xi_2),w_{mn}) &= \sum_{i=0}^{N}\sum_{j=0}^{N} u_{ij}\int_{-1}^{1}\int_{-1}^{1} J(\xi_1,\xi_2)\Psi_i(\xi_1)\Psi_j(\xi_2)\Psi_m(\xi_1)\Psi_n(\xi_2)d\xi_1 d\xi_2 \\ &= \sum_{i=0}^{N}\sum_{j=0}^{N}\sum_{p=0}^{N}\sum_{q=0}^{N} u_{ij}J(\xi_{1p},\xi_{2q})w_p w_q \delta_{ip}\delta_{mp}\delta_{jq}\delta_{nq} \\ &= \mathbf{w}_{pq}^T\mathbf{W}\mathbf{u},\end{aligned} \tag{A. 29}$$

where $\mathbf{W}$ is defined as $\mathbf{I}\mathbf{w}$ that $\mathbf{I}$ is the identity matrix of rank $(N+1)^2$. The vector in matrices $\mathbf{w}_{pq}$ is 1 at the pq-th component and 0 for others. As such, the inner product for trial functions can be expressed as $(u(\xi_1,\xi_2),w_{mn}) = \mathbf{W}\mathbf{u}$. Then the derivation of trial function is expressed as

$$\begin{aligned}(\nabla u(\xi_1,\xi_2),\nabla w) &= \left(\frac{\partial u}{\partial x},\frac{\partial w}{\partial x}\right)+\left(\frac{\partial u}{\partial y},\frac{\partial w}{\partial y}\right) \\ &= (\mathbf{D}_x\mathbf{u},\mathbf{D}_x\mathbf{w})+(\mathbf{D}_y\mathbf{u},\mathbf{D}_y\mathbf{w}) \\ &= \mathbf{D}_x^T\mathbf{W}\mathbf{D}_x\mathbf{u}+\mathbf{D}_y^T\mathbf{W}\mathbf{D}_y\mathbf{u} \\ &= \left(\mathbf{D}_x^T\mathbf{W}\mathbf{D}_x+\mathbf{D}_y^T\mathbf{W}\mathbf{D}_y\right)\mathbf{u}.\end{aligned} \tag{A. 30}$$

Let the τ to be the tangential direction, then we can express $\tau = \partial\Omega_e$ with its derivative being $\dfrac{\partial\tau}{\partial\xi} = \sqrt{\left(\dfrac{\partial x}{\partial\xi}\right)^2+\left(\dfrac{\partial y}{\partial\xi}\right)^2}$. Now, the left-hand side of Eq. (A. 19) can be expressed as

$$\begin{aligned}&\int_{\Omega_e}\left[\nabla\mathcal{N}_j(x)\cdot\nabla\mathcal{N}_i(x)+\lambda\,\mathcal{N}_j(x)\mathcal{N}_i(x)\right]\,d\Omega_e \\ &= \left(\mathbf{D}_x^T\mathbf{W}\mathbf{D}_x+\mathbf{D}_y^T\mathbf{W}\mathbf{D}_y+\lambda\mathbf{W}\right)\mathbf{u}\equiv\mathbf{A}_\mathbf{e}\mathbf{u},\end{aligned} \tag{A. 31}$$

where $\mathbf{D}_x^T\mathbf{W}\mathbf{D}_x+\mathbf{D}_y^T\mathbf{W}\mathbf{D}_y$ and $\mathbf{W}$ represent the stiffness and mass matrices, respectively. To expressed whole equation of Eq. (A. 19), we introduce the following

global operators for simplicity

$$-\int_{\Omega_e} f_{ij}\mathcal{N}_j(x)\mathcal{N}_i(x)\,d\Omega_e = -\mathbf{W}\mathbf{f}, \tag{A. 32}$$

$$\oint_{\partial\Omega_e} h_{ij}\mathcal{N}_j(x)\mathcal{N}_i(x)\,d(\partial\Omega_e) = \mathbf{B}\mathbf{h}, \tag{A. 33}$$

where

$\mathbf{f} = [f_{00}, f_{10}, \cdots, f_{N0}, f_{01}, f_{11}, \cdots, f_{NN}]^T$,

$$\mathbf{B} = \text{diag}\Bigg(w_0 w_0 \frac{\partial\tau}{\partial\xi_1}(\xi_0)\frac{\partial\tau}{\partial\xi_2}(\xi_0), w_1 w_0 \frac{\partial\tau}{\partial\xi_1}(\xi_1)\frac{\partial\tau}{\partial\xi_2}(\xi_0), \cdots, w_N w_0 \frac{\partial\tau}{\partial\xi_1}(\xi_N)\frac{\partial\tau}{\partial\xi_2}(\xi_0), w_N w_1 \frac{\partial\tau}{\partial\xi_1}(\xi_N)\frac{\partial\tau}{\partial\xi_2}(\xi_1), \cdots, w_N w_N \frac{\partial\tau}{\partial\xi_1}(\xi_N)\frac{\partial\tau}{\partial\xi_2}(\xi_N) \Bigg),$$

$\mathbf{h} = [h_{00}, h_{10}, \cdots, h_{N0}, h_{01}, h_{11}, \cdots, h_{NN}]^T$.

5. **Calculation of the coefficients**:

   In order to use global operators for simple expressions, we introduce matrix $\mathbf{G}$ by defining local $\mathbf{u_l}$ from $\mathbf{u_g}$ of the global degree of freedom (DOF) as

$$\mathbf{u_l} = \mathbf{G}\mathbf{u_g}. \tag{A. 34}$$

   Now, we rewrite and rearrange Eqs. (A. 31)-(A. 33) as

$$\mathbf{G}^T(\mathbf{A}_e \otimes \mathbf{I}_e)\mathbf{G}\mathbf{u}_g = -\mathbf{G}^T(\mathbf{W}_e \otimes \mathbf{I}_e)\mathbf{f}_e + \mathbf{G}^T(\mathbf{B}_e \otimes \mathbf{I}_e)\mathbf{h}_e, \tag{A. 35}$$

   where $\mathbf{I}_e$ represents the identity matrix of the rank that has the same number of total element number. To further simplify the system, let $\mathbf{A_g} = \mathbf{G}^T(\mathbf{A}_e \otimes \mathbf{I}_e)\mathbf{G}$ and $\mathbf{b_g} = -\mathbf{G}^T(\mathbf{W}_e \otimes \mathbf{I}_e)\mathbf{f}_e + \mathbf{G}^T(\mathbf{B}_e \otimes \mathbf{I}_e)\mathbf{h}_e$, then we have

$$\mathbf{A_g}\mathbf{u}_g = \mathbf{b_g}. \tag{A. 36}$$

Applying the Dirichlet B.C.s and expressing unknowns with superscripts $(\cdot)^{\mathrm{D}}$ and $(\cdot)^{\mathrm{u}}$, respectively, we can rearrange the above equation as

$$\begin{bmatrix} \mathbf{A} & \mathbf{A}^{\mathrm{D}} \\ 0 & \mathbf{I}^{\mathrm{D}} \end{bmatrix} \begin{bmatrix} \mathbf{u}_g^{\mathrm{u}} \\ \mathbf{u}_g^{\mathrm{D}} \end{bmatrix} = \begin{bmatrix} \mathbf{b}_g^{\mathrm{u}} \\ \mathbf{b}_g^{\mathrm{D}} \end{bmatrix}. \tag{A. 37}$$

Now, to obtain the coefficients, the following linear equation needs to be solved.

$$\mathbf{A}\mathbf{u}_g^{\mathrm{u}} = \mathbf{b}_g^{\mathrm{u}} - \mathbf{A}^{\mathrm{D}}\mathbf{u}_g^{\mathrm{D}} \equiv \mathbf{b}. \tag{A. 38}$$

A.3 Linear solver

The 2-D Helmholtz equation in the form of Eq. (A. 38) is applied for solving both the pressure and viscous substeps at each wavenumber. In particular, because of the large value of $1/\nu\Delta t$, the diagonal components of matrix $\mathbf{A}$ are dominant in viscous substeps during the solution procedure. Consequently, the preconditioned conjugate gradient (PCG) solver is employed. For parallel computing in the periodic direction, each of the 2-D Helmholtz equation is solved by sequence.

A.3.1 Solving the viscous substep

Equation (A. 38) can be split as $\mathbf{u_g}^{\mathrm{u}} = (\mathbf{I} - \mathbf{A})\mathbf{u_g}^{\mathrm{u}} + \mathbf{b}$. To iterate, the subscript is changed to the iterative number as $\mathbf{u}_{k+1}^{\mathrm{u}} = (\mathbf{I} - \mathbf{A})\mathbf{u}_k^{\mathrm{u}} + \mathbf{b}$ for $k = 0, 1, 2, \cdots$. Note that this equation satisfies the k-th Krylov subspaces $\mathcal{K}_k$. In order to ensure the best combination of u_k in $\mathcal{K}_k$, its residual $r_k = \mathbf{b} - \mathbf{A}\mathbf{u}_k$ needs to be orthogonal to $\mathcal{K}_k$. Simultaneously, the residual is required to have the minimal norm for u_k in $\mathcal{K}_k$. To achieve a faster convergence

rate, the preconditioning matrix $\mathbf{P}$ is applied

$$\begin{aligned}\mathbf{u}^{\mathrm{u}}_{k+1} &= (\mathbf{I}-\mathbf{A})\mathbf{u}^{\mathrm{u}}_{k}+\mathbf{b},\\ \mathbf{P}\mathbf{u}^{\mathrm{u}}_{k+1} &= (\mathbf{P}-\mathbf{A})\mathbf{u}^{\mathrm{u}}_{k}+\mathbf{P}\mathbf{b},\\ \mathbf{u}^{\mathrm{u}}_{k+1} &= \mathbf{u}^{\mathrm{u}}_{k}+\mathbf{P}^{-1}(\mathbf{b}-\mathbf{A}\mathbf{u}^{\mathrm{u}}_{k}),\end{aligned} \tag{A. 39}$$

Note that a Jacobi pre-conditioner is used in the substeps, i.e., $\mathbf{P} \equiv \mathrm{diag}(\mathbf{A})$. By taking the initial guess $\mathbf{u}_0$, then the iterations follows:

$r_0 = \mathbf{b} - \mathbf{A}\mathbf{u}_0$, $z_0 = \mathbf{P}^{-1} r_0$

Loop k**:**

$$\begin{aligned} w_k &= \mathbf{A} r_k && \%\\ \rho_k &= r_k^T z_k && \%\\ \alpha_k &= \frac{\rho_k}{w_k^T r_k} && \% \text{ Step length to next } u_k\\ \mathbf{u}_{k+1} &= \mathbf{u}_k + \alpha_k r_k && \% \text{ Approximate solution}\\ r_{k+1} &= r_k - \alpha_k w_k && \% \text{ Update the residual}\\ z_{k+1} &= \mathbf{P}^{-1} r_{k+1} && \% \text{ Update the correction}\\ \rho_{k+1} &= r_{k+1}^T z_{k+1} && \%\\ r_{k+1} &= z_{k+1} + \frac{\rho_{k+1}}{\rho_k} r_k && \% \end{aligned}$$

break if converged

End

A.3.2 Solving the pressure substep

To directly solve the pressure substep, the inverse matrix $\mathbf{A}^{-1}$ is involved which causes huge computing resources for storing memories, especially for DNS. Therefore, the Guyan condensation technique is employed to avoid this situation. Employing the Guyan condensation, the $\mathbf{u}$ is split into the primary and secondary DOF as $\mathbf{u}_p$ and $\mathbf{u}_s$, respectively. Now

our static equation $\mathbf{A}\mathbf{u} = \mathbf{b}$ can be expressed as

$$\begin{bmatrix} \mathbf{A}_{pp} & \mathbf{A}_{ps} \\ \mathbf{A}_{sp} & \mathbf{A}_{ss} \end{bmatrix} \begin{bmatrix} \mathbf{u}_p \\ \mathbf{u}_s \end{bmatrix} = \begin{bmatrix} \mathbf{b}_p \\ \mathbf{b}_s \end{bmatrix}. \tag{A. 40}$$

By multiplications, we can further obtain

$$\begin{bmatrix} \mathbf{A}_{pp} - \mathbf{A}_{ps}\mathbf{A}_{ss}^{-1}\mathbf{A}_{sp} & 0 \\ \mathbf{A}_{sp} & \mathbf{A}_{ss} \end{bmatrix} \begin{bmatrix} \mathbf{u}_p \\ \mathbf{u}_s \end{bmatrix} = \begin{bmatrix} \mathbf{b}_p - \mathbf{A}_{ps}\mathbf{A}_{ss}^{-1}\mathbf{b}_s \\ \mathbf{b}_s \end{bmatrix}, \tag{A. 41}$$

from which, it is straightforward that

$$\mathbf{u}_p = (\mathbf{A}_{pp} - \mathbf{A}_{ps}\mathbf{A}_{ss}^{-1}\mathbf{A}_{sp})^{-1}(\mathbf{b}_p - \mathbf{A}_{ps}\mathbf{A}_{ss}^{-1}\mathbf{b}_s). \tag{A. 42}$$

Now, the DOF has been reduced to $p \times p$, which has a significant low storage requirement. Furthermore, we can express $\mathbf{u}_s$ in terms of $\mathbf{u}_p$ as

$$\mathbf{u}_s = \mathbf{A}_{ss}^{-1}\mathbf{b}_s - \mathbf{A}_{sp}\mathbf{A}_{ss}^{-1}\mathbf{u}_p. \tag{A. 43}$$

Appendix: B

Derivation of Reynolds stress transportation equation

This appendix focuses on the detailed derivation of Reynolds stress transportation equation. Starting from the continuity equation ($\partial u_i/\partial x_i = 0$), and by applying Reynolds decomposition, we obtain

$$\left\langle \frac{\partial u_i}{\partial x_i} \right\rangle = \left\langle \frac{\partial \left(\langle u_i \rangle + u_i' \right)}{\partial x_i} \right\rangle = \left\langle \frac{\partial \langle u_i \rangle}{\partial x_i} \right\rangle + \cancel{\left\langle \frac{\partial u_i'}{\partial x_i} \right\rangle} = \left\langle \frac{\partial \langle u_i \rangle}{\partial x_i} \right\rangle = \frac{\partial \langle u_i \rangle}{\partial x_i} = 0, \quad \text{(B. 1)}$$

where the crossed term is zero due to time averaging. Then, the Naiver-Stokes equations can be rearranged to

$$\mathcal{NS}(u_i) = \frac{\partial u_i}{\partial t} + u_k \frac{\partial u_i}{\partial x_k} + \frac{1}{\rho} \frac{\partial p}{\partial x_i} - \nu \left(\frac{\partial^2 u_i}{\partial x_k \partial x_k} \right). \quad \text{(B. 2)}$$

Because $\mathcal{NS}(u_i)$ = 0, the following equation holds

$$\left\langle u_j' \mathcal{NS}(u_i) + u_i' \mathcal{NS}(u_j) \right\rangle = 0. \quad \text{(B. 3)}$$

As such, $u_j' \mathcal{NS}(u_i)$ can be expressed as

$$\begin{aligned}
u_j' \mathcal{NS}(u_i) &= u_j' \frac{\partial u_i}{\partial t} + u_j' u_k \frac{\partial u_i}{\partial x_k} + u_j' \frac{1}{\rho} \frac{\partial p}{\partial x_i} - u_j' \nu \left(\frac{\partial^2 u_i}{\partial x_k \partial x_k} \right) \\
&= u_j' \frac{\partial (\langle u_i \rangle + u_i')}{\partial t} + u_j' (\langle u_k \rangle + u_k') \frac{\partial (\langle u_i \rangle + u_i')}{\partial x_k} + u_j' \frac{1}{\rho} \frac{\partial (\langle p \rangle + p')}{\partial x_i} \\
&\quad - u_j' \nu \left[\frac{\partial^2 (\langle u_i \rangle + u_i')}{\partial x_k \partial x_k} \right] \\
&= u_j' \frac{\partial \langle u_i \rangle}{\partial t} + u_j' \frac{\partial u_i'}{\partial t} + u_j' \langle u_k \rangle \frac{\partial \langle u_i \rangle}{\partial x_k} + u_j' \langle u_k \rangle \frac{\partial u_i'}{\partial x_k} + u_j' u_k' \frac{\partial \langle u_i \rangle}{\partial x_k} + u_j' u_k' \frac{\partial u_i'}{\partial x_k} \\
&\quad + u_j' \frac{1}{\rho} \frac{\partial \langle p \rangle}{\partial x_i} + u_j' \frac{1}{\rho} \frac{\partial p'}{\partial x_i} - u_j' \nu \frac{\partial^2 \langle u_i \rangle}{\partial x_k \partial x_k} - u_j' \nu \frac{\partial^2 u_i'}{\partial x_k \partial x_k}.
\end{aligned} \tag{B. 4}$$

Following a similar process, $u_i' \mathcal{NS}(u_j)$ can be expressed as

$$\begin{aligned}
u_i' \mathcal{NS}(u_j) &= u_i' \frac{\partial \langle u_j \rangle}{\partial t} + u_i' \frac{\partial u_j'}{\partial t} + u_i' \langle u_k \rangle \frac{\partial \langle u_j \rangle}{\partial x_k} + u_i' \langle u_k \rangle \frac{\partial u_j'}{\partial x_k} + u_i' u_k' \frac{\partial \langle u_j \rangle}{\partial x_k} + u_i' u_k' \frac{\partial u_j'}{\partial x_k} \\
&\quad + u_i' \frac{1}{\rho} \frac{\partial \langle p \rangle}{\partial x_j} + u_i' \frac{1}{\rho} \frac{\partial p'}{\partial x_j} - u_i' \nu \frac{\partial^2 \langle u_j \rangle}{\partial x_k \partial x_k} - u_i' \nu \frac{\partial^2 u_j'}{\partial x_k \partial x_k}.
\end{aligned} \tag{B. 5}$$

From now on, the component form of Eq. (B. 3) will be used because the summation of the above equation is very lengthy. Starting with the unsteady terms, we obtain

$$\begin{aligned}
\left\langle u_j' \frac{\partial u_i}{\partial t} + u_i' \frac{\partial u_j}{\partial t} \right\rangle &= \left\langle u_j' \frac{\partial \langle u_i \rangle}{\partial t} + u_j' \frac{\partial u_i'}{\partial t} + u_i' \frac{\partial \langle u_j \rangle}{\partial t} + u_i' \frac{\partial u_j'}{\partial t} \right\rangle \\
&= \cancel{\left\langle u_j' \frac{\partial \langle u_i \rangle}{\partial t} \right\rangle} + \left\langle u_j' \frac{\partial u_i'}{\partial t} \right\rangle + \cancel{\left\langle u_i' \frac{\partial \langle u_j \rangle}{\partial t} \right\rangle} + \left\langle u_i' \frac{\partial u_j'}{\partial t} \right\rangle \\
&= \frac{\partial \langle u_i' u_j' \rangle}{\partial t}.
\end{aligned} \tag{B. 6}$$

Followed by the summation of convective terms, we obtain

$$\begin{aligned}
\left\langle u_j' u_k \frac{\partial u_i}{\partial x_k} + u_i' u_k \frac{\partial u_j}{\partial x_k} \right\rangle &= \left\langle u_j' \langle u_k \rangle \frac{\partial \langle u_i \rangle}{\partial x_k} + u_j' \langle u_k \rangle \frac{\partial u_i'}{\partial x_k} + u_j' u_k' \frac{\partial \langle u_i \rangle}{\partial x_k} + u_j' u_k' \frac{\partial u_i'}{\partial x_k} \right\rangle + \\
&\quad \left\langle u_i' \langle u_k \rangle \frac{\partial \langle u_j \rangle}{\partial x_k} + u_i' \langle u_k \rangle \frac{\partial u_j'}{\partial x_k} + u_i' u_k' \frac{\partial \langle u_j \rangle}{\partial x_k} + u_i' u_k' \frac{\partial u_j'}{\partial x_k} \right\rangle \\
&= \left\langle \cancel{u_j' \langle u_k \rangle \frac{\partial \langle u_i \rangle}{\partial x_k}} + u_j' \langle u_k \rangle \frac{\partial u_i'}{\partial x_k} + u_j' u_k' \frac{\partial \langle u_i \rangle}{\partial x_k} + u_j' u_k' \frac{\partial u_i'}{\partial x_k} \right\rangle + \\
&\quad \left\langle \cancel{u_i' \langle u_k \rangle \frac{\partial \langle u_j \rangle}{\partial x_k}} + u_i' \langle u_k \rangle \frac{\partial u_j'}{\partial x_k} + u_i' u_k' \frac{\partial \langle u_j \rangle}{\partial x_k} + u_i' u_k' \frac{\partial u_j'}{\partial x_k} \right\rangle \\
&= \langle u_k \rangle \frac{\partial \langle u_i' u_j' \rangle}{\partial x_k} + \langle u_j' u_k' \rangle \frac{\partial \langle u_i \rangle}{\partial x_k} + \langle u_i' u_k' \rangle \frac{\partial \langle u_j \rangle}{\partial x_k} + \frac{\partial \langle u_i' u_j' u_k' \rangle}{\partial x_k}.
\end{aligned} \tag{B. 7}$$

Then, sum up the pressure strain terms as

$$\begin{aligned}
\left\langle u_j' \frac{1}{\rho} \frac{\partial p}{\partial x_i} + u_i' \frac{1}{\rho} \frac{\partial p}{\partial x_j} \right\rangle &= \frac{1}{\rho} \left(\left\langle u_j' \frac{\partial \langle p \rangle}{\partial x_i} + u_j' \frac{\partial p'}{\partial x_i} + u_i' \frac{\partial \langle p \rangle}{\partial x_j} + u_i' \frac{\partial p'}{\partial x_j} \right\rangle \right) \\
&= \frac{1}{\rho} \left(\left\langle \cancel{u_j' \frac{\partial \langle p \rangle}{\partial x_i}} \right\rangle + \left\langle u_j' \frac{\partial p'}{\partial x_i} \right\rangle + \left\langle \cancel{u_i' \frac{\partial \langle p \rangle}{\partial x_j}} \right\rangle + \left\langle u_i' \frac{\partial p'}{\partial x_j} \right\rangle \right) \\
&= \frac{1}{\rho} \left(\left\langle u_j' \frac{\partial p'}{\partial x_i} \right\rangle + \left\langle u_i' \frac{\partial p'}{\partial x_j} \right\rangle \right) \\
&= \frac{1}{\rho} \left\langle \frac{\partial \left(p' u_j' \right)}{\partial x_i} - p' \frac{\partial u_j'}{\partial x_i} + \frac{\partial \left(p' u_i' \right)}{\partial x_j} - p' \frac{\partial u_i'}{\partial x_j} \right\rangle \\
&= \frac{1}{\rho} \left\langle \frac{\partial}{\partial x_k} \left(p' u_j' \delta_{ik} + p' u_i' \delta_{jk} \right) - 2 p' s_{ij}' \right\rangle \\
&= \frac{1}{\rho} \frac{\partial}{\partial x_k} \left(\langle p' u_j' \rangle \delta_{ik} + \langle p' u_i' \rangle \delta_{jk} \right) - \frac{2}{\rho} \langle p' s_{ij}' \rangle .
\end{aligned} \tag{B. 8}$$

Finally, the viscous terms summed together as

$$
\begin{aligned}
&-\left\langle u_j'\nu\left(\frac{\partial^2 u_i}{\partial x_k\partial x_k}\right)+u_i'\nu\left(\frac{\partial^2 u_j}{\partial x_k\partial x_k}\right)\right\rangle \\
&=-\left(\left\langle u_j'\nu\frac{\partial^2\langle u_i\rangle}{\partial x_k\partial x_k}\right\rangle+\left\langle u_j'\nu\frac{\partial^2 u_i'}{\partial x_k\partial x_k}\right\rangle+\left\langle u_i'\nu\frac{\partial^2\langle u_j\rangle}{\partial x_k\partial x_k}\right\rangle+\left\langle u_i'\nu\frac{\partial^2 u_j'}{\partial x_k\partial x_k}\right\rangle\right) \\
&=-\left(\cancel{\left\langle u_j'\nu\frac{\partial^2\langle u_i\rangle}{\partial x_k\partial x_k}\right\rangle}+\left\langle u_j'\nu\frac{\partial^2 u_i'}{\partial x_k\partial x_k}\right\rangle+\cancel{\left\langle u_i'\nu\frac{\partial^2\langle u_j\rangle}{\partial x_k\partial x_k}\right\rangle}+\left\langle u_i'\nu\frac{\partial^2 u_j'}{\partial x_k\partial x_k}\right\rangle\right) \\
&=-\left(\left\langle\frac{\partial}{\partial x_k}\left(u_j'\nu\frac{\partial u_i'}{\partial x_k}\right)\right\rangle-\left\langle\nu\frac{\partial u_j'}{\partial x_k}\frac{\partial u_i'}{\partial x_k}\right\rangle+\left\langle\frac{\partial}{\partial x_k}\left(u_i'\nu\frac{\partial u_j'}{\partial x_k}\right)\right\rangle-\left\langle\nu\frac{\partial u_i'}{\partial x_k}\frac{\partial u_j'}{\partial x_k}\right\rangle\right) \\
&=-\nu\frac{\partial^2\langle u_i'u_j'\rangle}{\partial x_k\partial x_k}+2\nu\left\langle\frac{\partial u_i'}{\partial x_k}\frac{\partial u_j'}{\partial x_k}\right\rangle.
\end{aligned}
\tag{B. 9}
$$

By substituting the results of Eqs. (B. 4) $-$ (B. 9) into Eq. (B. 3), we obtain

$$
\begin{aligned}
\left\langle u_j'\mathcal{NS}(u_i)+u_i'\mathcal{NS}(u_j)\right\rangle = {}& \frac{\partial\langle u_i'u_j'\rangle}{\partial t}+\langle u_k\rangle\frac{\partial\langle u_i'u_j'\rangle}{\partial x_k}+\langle u_j'u_k'\rangle\frac{\partial\langle u_i\rangle}{\partial x_k}+\langle u_i'u_k'\rangle\frac{\partial\langle u_j\rangle}{\partial x_k}+ \\
& \frac{\partial}{\partial x_k}\left(\langle u_i'u_j'u_k'\rangle\right)+\frac{1}{\rho}\frac{\partial}{\partial x_k}\left(\langle p'u_j'\rangle\delta_{ik}+\langle p'u_i'\rangle\delta_{jk}\right)-\frac{2}{\rho}\langle p's_{ij}'\rangle- \\
& \nu\frac{\partial^2\langle u_i'u_j'\rangle}{\partial x_k\partial x_k}+2\nu\left\langle\frac{\partial u_i'}{\partial x_k}\frac{\partial u_j'}{\partial x_k}\right\rangle=0.
\end{aligned}
\tag{B. 10}
$$

As time averaging, Eq. (B. 10) can be expressed as

$$
\begin{aligned}
&\underbrace{\langle u_k\rangle\frac{\partial\langle u_i'u_j'\rangle}{\partial x_k}}_{H_{ij}}-\underbrace{\left(-\langle u_j'u_k'\rangle\frac{\partial\langle u_i\rangle}{\partial x_k}-\langle u_i'u_k'\rangle\frac{\partial\langle u_j\rangle}{\partial x_k}\right)}_{P_{ij}}-\underbrace{\left(\frac{2}{\rho}\langle p's_{ij}'\rangle\right)}_{\Pi_{ij}}+\underbrace{\left(2\nu\left\langle\frac{\partial u_i'}{\partial x_k}\frac{\partial u_j'}{\partial x_k}\right\rangle\right)}_{\varepsilon_{ij}} \\
&\qquad-\underbrace{\left\{\frac{\partial}{\partial x_k}\left[-\langle u_i'u_j'u_k'\rangle-\frac{1}{\rho}\left(\langle p'u_j'\rangle\delta_{ik}+\langle p'u_i'\rangle\delta_{jk}\right)+\nu\frac{\partial\langle u_i'u_j'\rangle}{\partial x_k}\right]\right\}}_{D_{ij}}=0.
\end{aligned}
\tag{B. 11}
$$

where the under-braced terms read in order as the convection H_{ij}, the production, P_{ij}, the pressure strain, Π_{ij}, the viscous dissipation, ε_{ij}, and the total diffusion, D_{ij}. Specifically, total diffusion term D_{ij} is expressed as follows:

$$D_{ij} = -\frac{\partial \langle u_i' u_j' u_k' \rangle}{\partial x_k} - \frac{1}{\rho}\frac{\partial}{\partial x_k}\left(\langle p' u_j' \rangle \delta_{ik} + \langle p' u_i' \rangle \delta_{jk}\right) + \nu \frac{\partial^2 \langle u_i' u_j' \rangle}{\partial x_k \partial x_k} \quad . \tag{B. 12}$$

References

ADRIAN, R. J. 2007 Hairpin vortex organization in wall turbulence. *Phys. Fluids* **19** (4), 041301.

ADRIAN, R. J., MEINHART, C. D. & TOMKINS, C. D. 2000 Vortex organization in the outer region of the turbulent boundary layer. *J. Fluid Mech.* **422**, 1–54.

BHATIA, A. 2018 Principle of duct design in hvac systems. *Tech. Rep.*. Continuing Education and Development, Inc.

BLACKBURN, H. M. & SHEWIN, S. J. 2004 Formulation of a galerkin spectral element-fourier method for three-dimensional incompressible flows in cylindrical geometries. *J. Comp. Phys.* **197** (2), 759–778.

BRUNDRETT, E. & BAINES, W. D. 1964 The production and diffusion of vorticity in duct flow. *J. Fluid Mech.* **19** (3), 375–394.

DAI, Y.-J., HUANG, W.-X., XU, C.-X. & CUI, G.-X. 2015 Direct numerical simulation of turbulent flow in a rotating square duct. *Phys. Fluids* **27** (6), 065104.

DEISSLER, R.G. 1954 Analysis of turbulent heat transfer, mass transfer, and friction in smooth tubes at high prandtl and schmidt numbers. *NACA report, 1210* .

DEISSLER, R. G. & TAYLOR, M. F. 1956 Analysis of axial turbulent flow and heat transfer through banks of rods or tubes. In *Reactor heat transfer conference of* , p. 416.

DEL ÁLAMO, J. C. & JIMÉNEZ, J. 2003 Spectra of the very large anisotropic scales in turbulent channels. *Phys. Fluids* **15** (6), L41–L44.

FANG, X., YANG, Z., WANG, B.-C. & BERGSTROM, D. J. 2017 Direct numerical simulation of turbulent flow in a spanwise rotating square duct at high rotation numbers. *Int. J. Heat Fluid Flow* **63**, 88–98.

GAVRILAKIS, S. 1992 Numerical simulation of low-reynolds-number turbulent flow through a straight square duct. *J. Fluid Mech.* **244**, 101–129.

HARTNETT, J. P., KOH, J. C. Y. & MCCOMAS, S. T. 1962 A comparison of predicted and measured friction factors for turbulent flow through rectangular ducts. *ASME J. Heat Trans.* **84**, 82–88.

HEAD, M.R. & BANDYOPADHYAY, P. 1981 New aspects of turbulent boundary-layer structure. *J. Fluid Mech.* **107**, 297–338.

HOYAS, S. & JIMÉNEZ, J. 2006 Scaling of the velocity fluctuations in turbulent channels up to $Re_\tau = 2,003$. *Phys. Fluids* **18** (1), 011702.

HUSER, A. & BIRINGEN, S. 1993 Direct numerical simulation of turbulent flow in a square duct. *J. Fluid Mech.* **257**, 65–95.

HUSER, A., BIRINGEN, S. & HATAY, F. F. 1994 Direct simulation of turbulent flow in a square duct: Reynolds-stress budgets. *Phys. Fluids* **6** (9), 3144–3152.

JIMÉNEZ, J. 1998 The largest structures in turbulent wall flows. *In CTR Annual Research Briefs* pp. 943–945.

JIMÉNEZ, J. & MOIN, P. 1991 The minimal flow unit in near-wall turbulence. *J. Fluid Mech.* **225**, 213–240.

KARNIZDAKIS, G. E., ORSZAG, S. A. & ISRAELI, M. 1991 High-order splitting methods for the incompressible navier-stokes equations. *J. Comp. Phys.* **97**, 414–443.

KARNIZDAKIS, G. E. & SHEWIN, S. J. 2005 *Spectral/hp Element Methods for Computational Fluid Dynamics*, 2nd edn. New York, United States: Oxford University Press Inc.

KIM, J., MOIN, P. & MOSER, R. 1987 Turbulence statistics in fully developed channel flow at low reynolds number. *J. Fluid Mech.* **177**, 133–166.

LAUFER, J. 1951 Investigation of turbulent flow in a two-dimensional channel. *NACA, Report, No. 1053* .

MADABHUSHI, R. K. & VANKA, S. P. 1991 Large eddy simulation of turbulence-driven secondary flow in a square duct. *Phys. Fluids A* **3** (11), 2734–2745.

NIKURADSE, J. 1930 Untersuchungen über turbulente strömungen in nicht kreisförmigen rohren. *Ingenieur-Archiv* **1** (3), 306–332.

PATEL, V. C. & HEAD, M. R. 1969 Some observations on skin friction and velocity profiles in fully developed pipe and channel flows. *J. Fluid Mech.* **38**, 181–201.

PINELLI, A., UHLMANN, M., SEKIMOTO, A. & KAWAHARA, G. 2010 Reynolds number dependence of mean flow structure in square duct turbulence. *J. Fluid Mech.* **644**, 107–122.

PRANDTL, L. 1926 Über die ausgebildete turbulenz [turbulent flow]. *NACA, Tech Memo, No. 435* Translated by D. M. Miner, NACA.

RHIE, C. M. & CHOW, W.-L. 1983 Numerical study of the turbulent flow past an airfoil with trailing edge separation. *AIAA J.* **21** (11), 1525–1532.

ROBINSON, S. K. 1991 Coherent motions in the turbulent boundary layer. *Annu. Rev. Fluid Mech.* **23** (1), 601–639.

UHLMANN, M., PINELLI, A., KAWAHARA, G. & SEKIMOTO, A. 2007 Marginally turbulent flow in a square duct. *J. Fluid Mech.* **588**, 153–162.

VINUESA, R., NOORANI, A., LOZANO-DURÁN, A., EI KHOURY, G. K., SCHLATTER, P., FISCHER, P. F. & NAGIB, H. M. 2014 Aspect ratio effects in turbulent duct flows studied through direct numerical simulation. *J. Turbul.* **15** (10), 677–706.

YAO, J., ZHAO, Y.-L. & FAIRWEATHER, M. 2015 Numerical simulation of turbulent flow through a straight square duct. *Appl. Therm. Eng.* **91**, 800–811.

ZANG, T. A. 1991 On the rotation and skew-symmetric forms for incompressible flow simulations. *Appl. Numer. Math.* **7** (1), 27–40.

ZHOU, J.-G., ADRIAN, R. J., BALACHANDAR, S. & KENDALL, T. M. 1999 Mechanisms for generating coherent packets of hairpin vortices in channel flow. *J. Fluid Mech.* **387**, 353–396.